

# A Simple and Efficient Reconstruction Backbone for Snapshot Compressive Imaging

Jiamian Wang · Yulun Zhang · Xin Yuan · Yun Fu · Zhiqiang Tao

Received: date / Accepted: date

**Abstract** The emerging technology of snapshot compressive imaging (SCI) enables capturing high dimensional (HD) data in an efficient way. It is generally implemented by two components: an optical encoder that compresses HD signals into a single 2D measurement and an algorithm decoder that retrieves the HD data upon the hardware-encoded measurement. Over a broad range of SCI applications, hyperspectral imaging (HSI) and video compressive sensing have received significant research attention in recent years. Among existing SCI reconstruction algorithms, deep learning-based methods stand out as their promising performance and efficient inference. However, the deep reconstruction network may suffer from overlarge model size and highly-specialized network design, which inevitably lead to costly training time, high memory usage, and limited flexibility, thus discouraging the deployments of SCI systems in practical scenarios. In this paper, we tackle the above challenges by proposing a sim-

ple yet highly efficient reconstruction method, namely stacked residual network (SRN), by revisiting the residual learning strategy with nested structures and spatial-invariant property. The proposed SRN empowers high-fidelity data retrieval with fewer computation operations and negligible model size compared with existing networks, and also serves as a versatile backbone applicable for both hyperspectral and video data. Based on the proposed backbone, we first develop the channel attention enhanced SRN (CAE-SRN) to explore the spectral inter-dependencies for fine-grained spatial estimation in HSI. We then employ SRN as a deep denoiser and incorporate it into a generalized alternating projection (GAP) framework – resulting in GAP-SRN – to handle the video compressive sensing task. Extensive experimental results on hyperspectral and video datasets demonstrate the state-of-the-art performance, high computational efficiency, and flexibility of the proposed SRN on two SCI applications. Code and pre-trained models are available at [https://github.com/Jiamian-Wang/HSI\\_baseline](https://github.com/Jiamian-Wang/HSI_baseline).

**Keywords** Snapshot Compressive Imaging · Hyperspectral Imaging · Video Compressive Sensing · Residual Learning · Channel Attention · Iterative Optimization

## 1 Introduction

Snapshot compressive imaging (SCI) [1] captures the high-dimensional (HD) data in a hardware-encoding and software-decoding way. It is composed of an optical encoder to compress HD signals into 2D measurements and an algorithm decoder to retrieve the original signals with the hardware-encoded measurements. SCI systems are generally bandwidth/memory efficient and

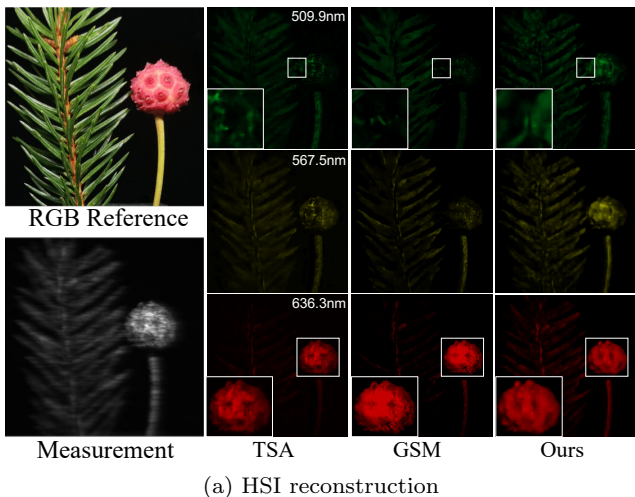
Jiamian Wang  
Department of Computer Science and Engineering, Santa Clara University, USA  
E-mail: JWang16@scu.edu

Yulun Zhang  
ETH Zürich, Switzerland  
E-mail: yulun100@gmail.com

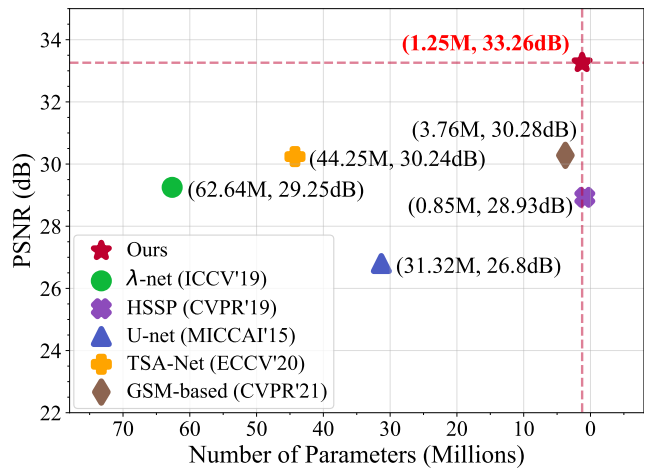
Xin Yuan  
Westlake University, Hangzhou, Zhejiang, China  
E-mail: xyuan@westlake.edu.cn

Yun Fu  
Department of ECE and Khoury College of Computer Science, Northeastern University, USA  
E-mail: yunfu@ece.neu.edu

Zhiqiang Tao  
Department of Computer Science and Engineering, Santa Clara University, USA  
E-mail: ztao@scu.edu



(a) HSI reconstruction



(b) Model comparison

Fig. 1: (a) Real HSI reconstruction of TSA-Net, GSM and the proposed method. The RGB reference (top-left) is shown to demonstrate the color. By comparison, the proposed method perceptually outperforms the other two on exemplar wavelengths. (b) Comparison between different methods in terms of PSNR ( $\uparrow$ ) and the model size ( $\downarrow$ ).

power-saving [1, 2, 3] and thus widely used in different scenarios, *e.g.*, temporal imaging [2, 4], light field microscopy [5], etc. Among various SCI applications, hyperspectral imaging and video compressive sensing have received significant research attention [6, 7, 8, 9] from the computer vision community in recent years.

Hyperspectral imaging (HSI) obtains multi-channel images which store visual primitives at discrete spectral wavelengths [10]. By conveying rich information, hyperspectral images could better describe the nature of scenes than traditional RGB images and exhibit advantages in a wide range of scenarios, such as object detection [11, 12], remote sensing [13, 14, 15], etc. In SCI, the hyperspectral data is encoded along the spectral axis and compressed into a measurement [16]. This could be done by the coded aperture snapshot spectral imaging (CASSI) system [7, 17], which is a mainstream optical design among existing works [17, 18, 19, 20].

Given the measurements by CASSI, many reconstruction algorithms [7, 8, 21, 22, 23, 24] have been proposed to retrieve hyperspectral images (Fig. 1a). For example, the optimization-based iterative methods [6, 25] obtain the estimations in modulated signal domains constrained by pre-defined regularizers [26, 27]. They can be concatenated with distinct optical encoders without the re-training procedure and potentially own high robustness to modulation patterns and noise. However, they usually suffer from a relatively high time complexity and low-fidelity performance [27]. The recent deep learning-based methods [7, 8, 23, 28] alleviate above issues by developing end-to-end reconstruction networks to directly approximate the solution of the inverse problem for SCI (*i.e.*, optical-encoded measurements  $\rightarrow$  hy-

perspectral images). While existing deep networks have achieved great success by yielding high-fidelity results with fast inference speed, their overlarge model size (considering limited hyperspectral images) and highly-specialized (only applicable to the HSI problem) network designs could lead to sub-optimal performance (see Fig. 1b) and narrow the application of a single reconstruction model on various SCI problems. To this end, the question *whether there exists a network design with competitive performance, small model size, and simple structure* raises for the emerging field of SCI.

In this work, we propose a simple yet highly-efficient reconstruction model, termed as stacked residual network (SRN), to address the above challenge (Fig. 2(c)). While the residual learning [29] has been used in the previous HSI works [7, 8, 30], we revisit it from two insights – nested structure and spatial-invariance. Specifically, we implement a nested network structure using multiple local skip connections governed by a global one, which well balances the network depth and limited training data. On the other hand, we design the network with a spatial-invariant learning property to linearly enlarge the receptive field towards high-fidelity reconstructions. Empirically, the proposed SRN achieves state-of-the-art performance with negligible amount of parameters compared with previous methods. Moreover, the computational operations of SRN could be further reduced by utilizing the downsampling/upsampling rescaling pairs for the HSI reconstruction network setup.

The proposed SRN is a versatile backbone that can be easily extended with advanced modules and is applicable to various SCI applications (*e.g.*, HSI and video compressive sensing). Particularly, we propose a novel

channel attention [31,32] enhanced SRN (CAE-SRN) to achieve a better computation/performance trade-off for the HSI problem. The channel attention provides more clues for spatial detail restoration from the scope of the spectral dimension by considering the channel-inter-dependencies, compensating for the missing details without overburdening the network. By the experiment, the proposed CAE-SRN clearly improves over SRN with the rescaling pairs included (see Table 3).

Besides HSI, we also apply the proposed backbone SRN in another mainstream SCI application – video compressive sensing. Similarly, the sensing procedure also follows an encoding-decoding fashion. The coded aperture compressive temporal imaging (CACTI) [2] is a representative SCI encoder to compress the video frames into a 2D measurement. For the decoding, existing methods can be divided into three categories. 1) The optimization-based iterative methods [6,33,34,35] solve the inverse problem by designing novel regularizers and solvers. 2) Deep reconstruction methods [36,37] directly learn the mapping from a 2D measurement to temporal frames. For example, the recent proposed BIRNAT [36] is capable to retrieve a  $256 \times 256 \times 8$  video data within 200ms and perceptually outperforms previous counterparts. 3) The hybrid methods that combine iterative algorithms and deep networks, *i.e.*, deep unfolding [27,38] and plug-and-play (PnP) [37,39] models.

However, bearing the goal of *faithfully retrieving high-speed videos in real-time*, existing methods may show limitations in one way or another. On the one hand, the optimization-based iterative methods are a bit too slow, *i.e.*, DeSCI requires over 6000s to reconstruct a  $256 \times 256 \times 8$  data. On the other hand, deep reconstruction networks are efficient but cannot comply with the general speed requirement, *i.e.*, 30 fps, due to the large model size. In contrast, the hybrid method appears to be a promising direction. For example, the recent proposed GAP-net [27] yields competitive performance with tens of times faster inference speed (<10ms) than BIRNAT [36] on the same platform. While the GAP-net serves as one of the fastest SCI decoding algorithms (allowing >60 fps video retrieval theoretically), its deep reconstruction network usually sets a performance bottleneck due to the lack of lightweight backbones. In light of this, we develop GAP-SRN for the video compressive sensing task by incorporating SRN into the generative alternating projection [27,40] framework. Specifically, SRN works as a “deep denoiser” for GAP, and its simple structure and efficient property facilitate the iterative optimizing procedure. By unfolding multiple SRN entities, the proposed GAP-SRN could explicitly exploit the temporal and spatial correlations in modulated signal domains.

To sum up, we provide a new deep reconstruction backbone for SCI in the spectral and video contexts. We summarize the contribution of this work in four-folds.

- A simple yet highly-efficient SCI reconstruction network is provided by revisiting the residual learning strategy, which could be used as a faithful reconstruction backbone for further modulations.
- Based on the proposed backbone, a novel CAE-SRN has been provided for HSI, which effectively retrieves the visual primitives by exploiting the spectral inter-dependencies. Besides, the model not only demonstrates high robustness to optical encoders, but also, to our best knowledge, empowers high-resolution spectral data retrieval for the first time.
- By integrating the proposed backbone into the generalized alternating projection (GAP) framework, we proposed a novel GAP-SRN that iteratively conducts the linear projection and SRN-based signal estimation for the task of the video compressive sensing. Owing to the fast inference and effectiveness of the proposed SRN, we make a solid step toward real-time high-speed video reconstruction.
- Extensive experimental results on both hyperspectral and video datasets demonstrate the state-of-the-art performance of the proposed methods upon SRN and reveal the versatility of this proposed backbone on both popular applications of SCI.

The organization of this paper is as follows. In Section 2, the related works of SCI on both applications are outlined. In Section 3, we introduce the mathematical background of SCI and propose the backbone, stacked residual network (SRN). We further describe the CAE-SRN for HSI and GAP-SRN for video reconstruction. In Section 4, we perform extensive experiments to verify the effectiveness of proposed methods on above applications, respectively. Finally, we draw the conclusion and discuss the future work in Section 5.

## 2 Related Work

This study focuses on two popular applications hyperspectral imaging (HSI) and video compressive sensing based on spectral and video SCI systems, respectively.

### 2.1 Spectral SCI

For spectral SCI, the coded aperture snapshot spectral imager (CASSI) is provided as a promising detecting instrument due to its convenience in optical alignment and simplicity in spectral projection [3]. It firstly encodes the hyperspectral data upon specific wavelengths

via multiple masks (*i.e.*, shifted version of a single coded aperture). Then it projects the signal onto a 2D measurement via a disperser. Following this, many software-based reconstruction algorithms are proposed upon advanced compressive sensing (CS) algorithms [41, 42].

Previously, iterative-based algorithms demonstrate promising reconstruction performance. To obtain desired results, diverse priors are employed as regularization terms, constraining the optimization space for the iteration. For example, [43] solves the problem through wavelet-based regularization, the GPSR [44] applies the sparse prior for reconstruction. The TV priors are included in TwIST [25] and GAP-TV [24]. Among iterative-based algorithms, DeSCI [6] sets the state-of-the-art performance by proposing a novel framework under the flow of rank minimization. Despite the prosperity of iterative-based algorithms, challenges like long reconstruction time (*i.e.*, DeSCI requires more than an hour for an  $256 \times 256 \times 8$  data reconstruction) and potentially unstable convergence still exist.

By comparison, recently well-explored deep learning (DL)-based methods are characterized by fast reconstruction (*i.e.*, the inference time is always at second-level) and simultaneously, high retrieval performance. They seek to solve the problem from different perspective of views. The  $\lambda$ -net [8] trains a dual-stage reconstruction model under the framework of the generative adversarial network. The TSA-Net [7] explores the spectral and spatial self-attentions in an order-independent manner for the first time, achieving impressive reconstruction performance since proposed. The GSM [28] method proposes a Maximum a Posterior (MAP) estimator upon learnable Gaussian Scale Mixture (GSM) prior, with included sub-modules embodied by deep neural networks. It yields the best performance among concurrent reconstruction algorithms. The prevalence of the DL techniques facilitate the wide deployment of SCI systems to diverse real-world applications. However, the heavy computation burden and long training time induced by the large model size prohibit such a development. Also, it is inconvenient to make further modifications on existing highly-specialized network structures, setting up barriers to the future works.

To mitigate these problems, one practical solution is to integrate the advantages of deep neural networks and iterative-based methods. This leads to twofold popular frameworks: 1) deep unfolding (unrolling) methods, which conducts optimization iterations upon a series of concatenated deep neural networks, *i.e.*, GAP-net [27] and HSSP [30]. Since linear projections are conducted between the networks (stages), one can flexibly expand or shrink the whole framework. 2) Plug-and-play (PnP) frameworks [9, 45], which treat the pre-trained neural

networks as deep denoisers in the iterative-based algorithms. Both deep unfolding and PnP methods could be flexibly modulated. They also simultaneously benefit from iterative operations and learning capacity of undetermined neural network settings. Related methods are expected to be relatively light weight (as compared in Fig. 1b, HSSP only contains less than 1M parameters) and demonstrate the robustness to masks [27].

On the other hand, a more direct solution of improving the underlying flexibility and efficiency is to introduce lightweight and simple-structured networks as reconstruction backbones, which could be either solely used or conjointly integrated into other frameworks. A popular option is the U-Net [46]. For example, the TSA-Net [7] builds upon U-Net structure. The GSM [28] employing U-Net for the regularization parameter approximation and the prior local mean estimation. The GAP-net [27] with U-Net leads to a pleasing results. However, the low-fidelity performance (*i.e.*,  $<27$ dB by PSNR) of solely-used U-Net reveals that its inherently limited ability in processing hyperspectral data.

Notably, the residual learning [29] strategy beneath the U-Net structure serves as another popular schema for deep network design [8, 27, 30] in SCI. However, none of existing works truly exploit the underlying potential of the schema. Based on this observation, we take advantage of the residual learning by further proposing a nested structure with a spatial-invariant characteristic.

## 2.2 Video SCI

For video SCI, the coded aperture compressive temporal imaging (CACTI) compresses the high-speed scenes at a lower capture rate [2]. Firstly, CACTI uses an objective lens to take the temporal frames. They are further encoded by physical masks with different spatial patterns displayed on the digital micromirror device (DMD). Finally, the monochrome/color CCD detects the 2D measurement that contains the information of the corresponding compressed signal.

For the video frame reconstruction, existing algorithms can be similarly categorized into three groups: 1) model-based methods, among which the DeSCI [47] benefits from the weighted nuclear norm minimization (WNNM) [48] and alternating direction method of multipliers (ADMM) solver [49], delivering the most promising performance. 2) Deep neural networks directly learn a straightforward mapping from the measurement to video frames. For example, the E2E-CNN [37] supports millisecond-level retrieval speed. The BIRNAT [36] employs a recurrent neural network to explore the correlation between the video frames. Also, empowered

by adversarial training, this novel method perceptually outperforms existing methods. 3) Unfolding and PnP-based methods form another popular stream. Recently, a PnP-FFDNet [50] that takes the FFDNet [51] as the denoiser achieves promising performance with second-level retrieval time on  $256 \times 256 \times 8$  video data retrieval. However, the capacity of the pre-trained denoiser sets the bottleneck for this method. By comparison, the GAP-net [27] demonstrates more descent results by flexibly integrating proper denoiser among several candidates including AutoEncoders, U-nets and ResNets etc., by training from scratch.

### 3 Methodology

#### 3.1 Mathematical Model of SCI

**Forward Model.** The forward encoding process of SCI can be expressed via a unified mathematical model. In this work we take the 3D data (spectral data or video frames) as an example. Given the cube  $\mathbf{F} \in \mathbb{R}^{N_x \times N_y \times N_c}$  where  $N_x$ ,  $N_y$ , and  $N_c$  represent the height, width and number of channels (frames), respectively. The 2D measurement  $\mathbf{Y}$  is obtained by modulating data cube with masks  $\mathbf{M} \in \mathbb{R}^{N_x \times N_y \times N_c}$  along the target dimension as

$$\mathbf{Y} = \sum_{n_c=1}^{N_c} \mathbf{F}(:, :, n_c) \odot \mathbf{M}(:, :, n_c) + \mathbf{G}, \quad (1)$$

where  $\mathbf{G}$  denotes a 2D measurement noise and  $\odot$  is the Hadamard product. Notably, the  $N_c$  in Eq. (1) could refer to the number of wavelength ( $N_\lambda$ ) in spectral SCI or the number of temporal frames ( $N_t$ ) for compression in video compressive sensing. The forward model of SCI can be alternatively expressed in vector domain by  $\mathbf{f} = \text{vec}([\mathbf{f}^{(1)} \dots \mathbf{f}^{(N_c)}])$  where  $\mathbf{f}^{(n_c)} = \text{vec}(\mathbf{F}(:, :, n_c))$  and similarly determining the sensing matrix

$$\Phi = [\mathbf{D}_1, \dots, \mathbf{D}_{N_c}], \quad (2)$$

where  $\mathbf{D}_{n_c} = \text{Diag}(\text{vec}(\mathbf{M}(:, :, n_c)))$ . To this end, a vectorized forward model could be yield as

$$\mathbf{y} = \Phi \mathbf{f} + \mathbf{g}. \quad (3)$$

In the following, we will deploy this generalized forward model in CASSI and CACTI for hyperspectral imaging and video compressive sensing, respectively.

**CASSI for Spectral SCI.** The spectral SCI is specifically associated with the the spectral data corresponding to numerous wavelengths. Regarding this, a prevailing spectral imager, CASSI, employs a fixed 2D coded aperture (mask) plus a disperser, which is equivalent to different masks, leading to a passive modulation. Here

we use  $N_\lambda$  exchange  $N_c$ . For aforementioned spectral data  $\mathbf{F}$ , we firstly compute signal modulation implemented by the mask in a channel-wisely way as

$$\mathbf{F}'(:, :, n_\lambda) = \mathbf{F}(:, :, n_\lambda) \odot \mathbf{M}^*, \quad (4)$$

where  $\mathbf{F}' \in \mathbb{R}^{N_x \times N_y \times N_\lambda}$  denotes the modulated signals,  $\mathbf{M}^* \in \mathbb{R}^{N_x \times N_y}$  refers to a pre-defined physical mask,  $n_\lambda \in [1, \dots, N_\lambda]$  indexes wavelengths. By passing to a single disperser (SD), the  $\mathbf{F}'$  is tilted and sheared along the  $y$ -axis. Let  $\mathbf{F}'' \in \mathbb{R}^{N_x \times (N_y + N_\lambda - 1) \times N_\lambda}$  be the tilted cube, and  $\lambda_c$  be a reference wavelength, *i.e.*,  $\mathbf{F}'[:, :, n_{\lambda_c}]$  works like an anchor image without shearing and

$$\mathbf{F}''(u, v, n_\lambda) = \mathbf{F}'(x, y + d(\lambda_n - \lambda_c), n_\lambda), \quad (5)$$

where  $(u, v)$  locates the coordinate system on the detector plane,  $\lambda_n$  denotes the  $n_\lambda$ -th channel,  $\lambda_c$  refers to the anchored wavelength, and  $d(\lambda_n - \lambda_c)$  represents a spatial shift of the  $n_\lambda$ -th channel. We further have

$$\mathbf{Y} = \sum_{n_\lambda=1}^{N_\lambda} \mathbf{F}''(:, :, n_\lambda) + \mathbf{G}, \quad (6)$$

where  $\mathbf{Y} \in \mathbb{R}^{N_x \times (N_y + N_\lambda - 1)}$  is the measurement and  $\mathbf{G} \in \mathbb{R}^{N_x \times (N_y + N_\lambda - 1)}$  denotes the measurement noise. Combining the mask encoding in Eq. (4) and shifting in Eq. (5), we express the passive modulation as

$$\begin{aligned} \mathbf{M}(u, v, n_\lambda) &= \mathbf{M}^*(x, y + d(\lambda_n - \lambda_c)), \\ \tilde{\mathbf{F}}(u, v, n_\lambda) &= \mathbf{F}(x, y + d(\lambda_n - \lambda_c), n_\lambda). \end{aligned} \quad (7)$$

By substituting original data cube in Eq. (1) with  $\tilde{\mathbf{F}}$ , the measurement  $\mathbf{Y}$  obtained in Eq. (6) becomes

$$\mathbf{Y} = \sum_{n_\lambda=1}^{N_\lambda} \tilde{\mathbf{F}}(:, :, n_\lambda) \odot \mathbf{M}(:, :, n_\lambda) + \mathbf{G}. \quad (8)$$

The subsequent vectorization of  $\mathbf{Y}$  exactly follows the unified model. Notably, the sensing matrix  $\Phi$  given in Eq. (2) has a very special structure that most existing well-developed CS theories [52, 53] cannot easily handle, *i.e.*,  $\Phi$  is not only a fat matrix but also highly sparse — it is composed of  $N_\lambda$  concatenated diagonal matrices with at most  $nN_\lambda$  nonzero elements.

Given the measurement  $\mathbf{y}$  captured by the SD CASSI system, the reconstruction is to solve  $\mathbf{f}$  used in Eq. (3), falling in the vein of inverse problem [16]. Since the sparse sensing matrix  $\Phi$  is determined by the masks, deep reconstruction networks like TSA-Net [7] firstly discretizes the input measurement by shifted version of masks. Following the same procedure, we assume that the underlying mapping is more inclined to identity relationship, yielding a residual learning skeleton.

**CACTI for Video SCI.** In contrast with the spectral SCI, video SCI refers to capturing high-speed video

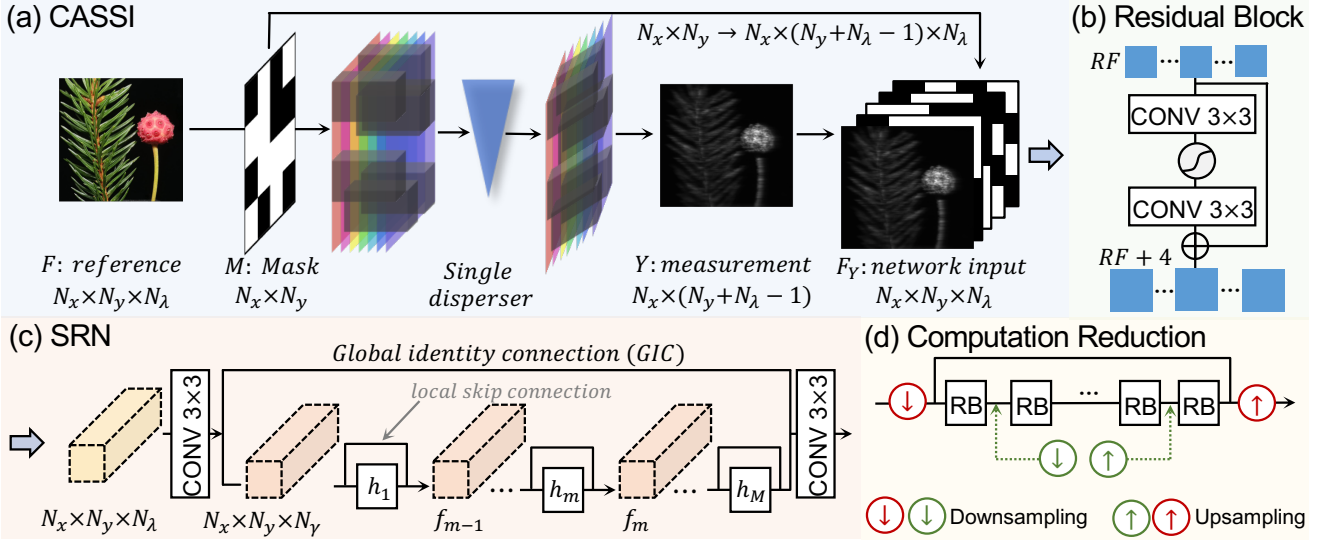


Fig. 2: CASSI compression and software-based reconstruction for spectral SCI. Note that we exchange  $N_c$  with  $N_\lambda$ . (a) In CASSI, a 2D coded aperture (mask)  $M$  encodes the HSI signal  $F$  at specific wavelengths. A disperser shears the signal along the y-axis. The Network input  $F_Y$  is initialized by measurement and shifted version of the mask. (b) Structure of the residual block. (c) Architecture of the SRN. It is characterized by nested residual learning and spatial-invariant learning. (d) Computation reduction through rescaling pairs, which can be flexibly plugged into the network. we use 2-paired rescaling as an example.

frames at a lower capture rate by the compressive imaging system, *i.e.*, CACTI. Different from the CASSI, CACTI directly applies shifting masks or variant patterns on the digital micromirror device (DMD), resulting in an activate modulation. Due to this, it acts as a low-power imager by skipping code transmission during the signal modulation [2]. As the CACTI and CASSI functionally work in the same way, one can directly refer to the generalized forward model for video SCI.

### 3.2 A Simple SCI Reconstruction Backbone by SRN

In this section, we introduce the proposed stacked residual network (SRN) in detail. Despite the simple structure, it effectively exploits the potential of nested residual learning (NRL) and benefits from the characteristic of spatial-invariant learning. By employing rescaling pairs, we make a further step on computation reduction, yielding a light-weight and highly-efficient model.

For better illustration, we introduce the backbone under the application of spectral SCI. Firstly the hyperspectral signal is captured by the optical apparatus with a SD CASSI system [7]. As demonstrated in Fig. 2 (a), the 3D signal corresponding to a given real-world (or synthetic) scene is compressed by a 2D measurement  $Y$ . We use  $F_Y \in \mathbb{R}^{N_x \times N_y \times N_\lambda}$  as the initialized input for the network and define its  $n_\lambda$ -th channel as

$$F_Y[:, :, n_\lambda] := \text{shift}(M_{n_\lambda} \odot Y), \quad (9)$$

where *shift* modulates the product result back to original spatial dimension of HSI data. Overall, the reconstruction mapping is obtained by

$$f_{SRN}(\cdot) : F_Y \rightarrow \hat{F}, \quad (10)$$

where  $\hat{F}$  denotes the reconstruction result. Essentially, the proposed SRN  $f_{SRN}(\cdot)$  learns to fit  $\Phi^{-1}$  expressed in a vector space given in Eq. (3).

As shown in Fig. 2 (c), the majority of the SRN is the nested residual learning module. This requires the residual output shares the same dimension as the network input in the spectral domain. Therefore, directly employing the NRL poses a large limitation to the network width and potentially compromise the learning capacity [54]. Therefore, we create feature embedding with manipulated spectral channels by implementing CONV layers:  $\mathbb{R}^{N_x \times N_y \times N_\lambda} \rightarrow \mathbb{R}^{N_x \times N_y \times N_\gamma}$ . Conversely, spectral channels are recovered after the NRL.

#### 3.2.1 Nested Residual Learning

It is widely known that the network depth contributes to the modeling ability [55], but poses obstacles to the training on the other hand [54]. Putting emphasize on nested residual learning upon global identity connection and local skip connections (LSCs) ensures the flexible gradient propagation within the network [56].

For the residual mapping part, we concatenate multiple Residual Blocks (RBs) governed by local skip connections separately. By doing this, one can customize

the network structure adapting to different SCI applications, which makes the SRN differentiate from other deep models with deterministic architectures. No matter how many RBs are employed, the network remains well organized and transductive. The feed-forward operation between RBs is proceeded as

$$f_m = H_m(f_{m-1}) = h_m(f_{m-1}) + f_{m-1}, \quad (11)$$

where  $H_m(\cdot)$  denotes the residual learning given by a CONV-ReLU-CONV structure with a local skip connection, *i.e.*,  $H_m(x) = \text{CONV}(\text{ReLU}(\text{CONV}(x))) + x$ , and  $f_{m-1}$  represents the output of the  $(m-1)$ th Residual Block. Supported by experimental results, we remove the Batch Normalization [57] in RBs. The whole stacked residual part could be represented as

$$f_M = H_M(H_{M-1}(\dots H_2(H_1(f_0)) \dots)), \quad (12)$$

where  $f_0$  is given as the feature embedding before NRL. Thus, we could treat all the RBs in Eq. (12) as a spatial / spectral-invariant mapping  $f_M : \mathbb{R}^{N_x \times N_y \times N_\lambda} \rightarrow \mathbb{R}^{N_x \times N_y \times N_\lambda}$ , and define the reconstruction model as

$$f_{SRN} = \text{CONV}(f_M(\text{CONV}(\mathbf{F}_Y)) + \text{CONV}(\mathbf{F}_Y)). \quad (13)$$

Overall, such a simple and well-organized and network structure shares similar principles with existing residual-based reconstruction models but is characterized by intertwined residual hierarchies, thus fully exploits the potential of the residual learning schema.

### 3.2.2 Spatial-invariant Learning

The usage of multiple Residual Blocks not only enables arbitrary network depth, also benefits the architecture customization from the perspective of receptive field (RF), which can be generally enlarged by stacking more layers. The RF should be sufficiently large to capture the semantic information for tasks like image classification and segmentation [58]. However, trade-offs need to be made considering the input image size, potential size of relevant area and computation burden. One can easily measure the RF of the SRN since the area is linearly increased with more RBs. This is implemented by the same kernel size and padding operation in Residual Blocks (Fig. 2 (b)), leading to the *spatial-invariant learning* – the spatial output size of all the RBs are the same in the proposed SRN backbone. Fig. 3 shows the comparison of RF between SRN and the U-net backbone. Given the  $256 \times 256 \times 28$  HSI data, the consequent RF of SRN is  $70 \times 70$ , which is proven to be sufficiently large for a compelling performance. While that of the U-Net is over  $500 \times 500$ , which turns out that barely contributes to the reconstruction performance but takes more computational resource (see Table 3).

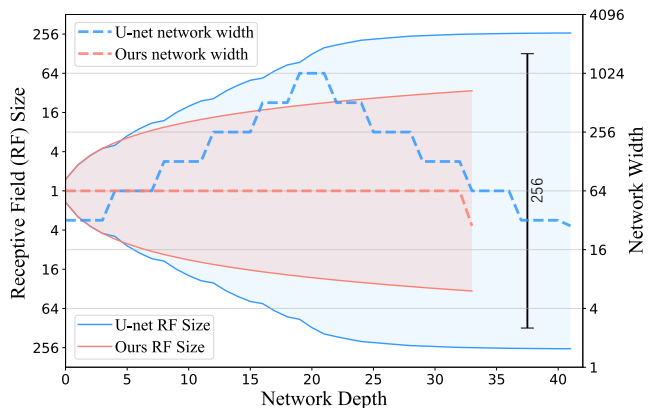


Fig. 3: Receptive field (RF) size and network width comparison plotted in Log-scale (U-Net [8] v.s. Ours). The RF of our method could be linearly extended with a salable structure. Compared with that of the U-Net (*i.e.*,  $532 \times 532$ ), we find RF of  $70 \times 70$  is sufficiently large given input of  $256 \times 256$  (black bar). Besides, the network width of SRN simply remains invariant.

Notably, the network width (channels of network embedding)  $N_\gamma$  also remains invariant across the NRL module, as demonstrated in Fig. 3. Particularly, we set the  $N_\gamma$  to be much larger than the number of initial spectral channels  $N_\lambda$  (*i.e.*, 64 v.s. 28) to increase the spectral-wise redundancy of intermediate embedding.

### 3.2.3 Computational Efficiency Enhancement

In this work, we measure the computation burden by floating point operations (FLOPs), *i.e.*, the amount of additions and multiplications. Larger model with larger input spatial size generally end up with high FLOPs. In addition, both the larger model size and the higher FLOPs indicate more GPU memory usage. Despite the small model of proposed SRN, the computation included is still significant. As compared in Table 3, the SRN taking 3% parameters of TSA-Net contains similar computation instead. This indicates the underlying computation time and resource occupation still remain considerable, which limits the future deployment of SRN in diverse scenarios. Take the high-resolution HSI (HR-HSI) reconstruction as an example. Existing deep reconstruction networks set demanding requirements to the GPU memory, therefore rarely visualizing reconstruction from HR-HSI over 1000 pixel scale. Aiming at efficient and power-saving reconstruction, we seek to reduce computation burden of SRN.

We consider simply introducing rescaling pairs for the objective. It essentially contains a downsampling operation for a leap upon receptive fields and an up-sampling operation exactly doing the inverse. By pro-

cessing feature maps with much smaller spatial size inclusively, one can diminish the computation without disturbing key learning elements (*i.e.*, model size, network depth). Another advantage is that the pairs can be flexibly plugged in the salable network structure, providing more options over network design. We implement the downsampling operation with CONV layer at a specific stride. For upsampling, we use famous *PixelShuffle* [59] instead of traditional interpolations or deconvolution. Specifically, the operation can be expressed as  $\mathbb{R}^{H \times W \times C r^2} \rightarrow \mathbb{R}^{Hr \times Wr \times C}$  with upsampling scale  $r$ .

As shown in Fig. 2 (d), rescaling pairs can be directly inserted between Residual Blocks. The larger span between down/up-sampling, the more computation mitigated. In this work, we try two different cases. Based on the original SRN (dubbed as SRN(v1)), we let the rescaling pair with scale 2 right outside the NRL module. Based on this variant, we further introduce one more rescaling pair in the NRL, *i.e.*, includes  $K$  RBs in the middle, yielding SRN(v3). From experiment results, we observe that three variants lead to the state-of-the-art/competitive performance under simulation data (refer to Table 1), while the performance will descend with more rescaling pairs. This is due to the lossy compression by the downsampling. In the following we will alleviate this problem via channel attention technique.

### 3.3 CAE-SRN for Spectral SCI

How to make up for the informative detail loss by rescaling pairs? Previous works provide a possible solution by revealing main channel features [31]. That is to say, better reconstruction can be obtained by differentiating the importance of channels, under missed visual descriptions. In single image denoising, empirical evidence indicates that the attention guided scaling [32] alleviates the obstacle of informative loss. Inspired by this, we signify the channel importance by channel attention enhancement (CAE) module into Residual Blocks.

The main idea is to explicitly discriminate  $N_\gamma$  channels according to the inter-dependency and informative abundance [60]. As shown in Fig. 4. Given the input  $f_{m-1} \in \mathbb{R}^{N_x \times N_y \times N_\gamma}$  of the  $m$ -th Residual Block,  $r_{m-1}$  represents the original residual output as  $r_{m-1} = \text{CONV}(\text{ReLU}(\text{CONV}(f_{m-1})))$ . We initialize the channel attention  $a$  by global average pooling as

$$a[n_\gamma] = \frac{1}{H_{m-1} W_{m-1}} r_{m-1}[:, :, n_\gamma], \quad (14)$$

where  $n_\gamma = 1, \dots, N_\gamma$ . Next, we fuse channel informative degrees and determine CAE according to the dependency, implemented by

$$a \leftarrow \text{CONV-sigmoid}(\text{CONV-ReLU}(a)). \quad (15)$$

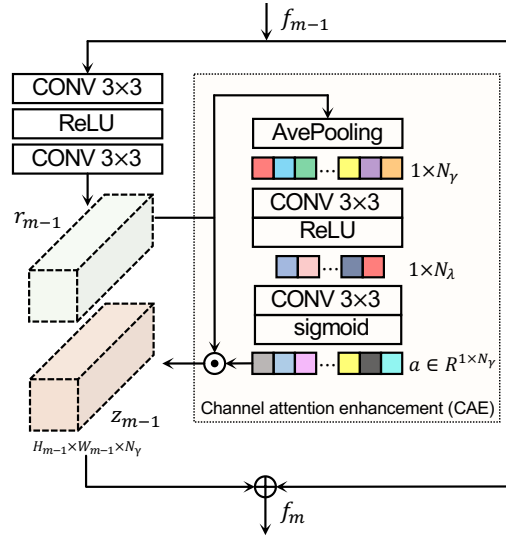


Fig. 4: Details of channel attention enhancement (CAE). The Residual Block governs the CAE module. The CAE vector  $a$  is computed by exploiting channel informative details (via global average pooling) and channel dependencies learned by nonlinear representation (via CONVs and activation functions).

The attention makes effect by multiplication

$$z_{m-1}[:, :, n_\gamma] = a[n_\gamma] \odot r_{m-1}[:, :, n_\gamma], \quad (16)$$

where  $z_{m-1}[:, :, n_\gamma]$  is the CAE-residual. Finally, we obtain the output of RB by  $f_m = f_{m-1} + z_{m-1}$ . In original SRN, all residual channels are equally accounted in each RB. By channel attention enhancement, more possibilities could be exploited in a spectral-wise, potentially compensating for the spatial informative detail deficiency. Consistently, we indeed observe obvious performance boosts on SRN(v2) and SRN(v3) with CAE.

**Model Training.** The proposed CAE-SRN is trained to minimize a mean squared error (MSE) between the ground truth HSIs and reconstruction results

$$\mathcal{L}_{MSE}(\phi) = \frac{1}{N} \sum_{n=1}^N \|\hat{\mathbf{F}}_n - \mathbf{F}_n\|^2, \quad (17)$$

where  $\hat{\mathbf{F}} = f_{\text{CAE-SRN}}(\mathbf{F}_Y)$  is given in Eq. (13) and  $N$  is the number of samples.  $\phi$  denotes all the parameters.

For simulation, synthetic hyperspectral images are fed into the SD CASSI for input initialization according to Eq. (9). Therefore, the original 3D cube naturally becomes the ground truth (GT). For real-world HSI reconstruction, training is conducted upon the simulation training set plus imposing Gaussian noise on the measurements to mimic real-captured measurements. We uniformly sample the standard deviation (std) from  $[0, 0.05]$ , and employ the measurements generated by a real SD CASSI system to the trained model.



### 3.4 GAP-SRN for Video SCI

As a versatile network design for SCI reconstruction, not only the proposed SRN enables outstanding retrieval performance in the application of hyperspectral imaging, it also could be effectively leveraged for video compressive sensing as a promising backbone. Specifically, we integrate the SRN into a popular unfolding framework of SCI, namely generalized alternating projection (GAP) [40]. Following the previous attempts of deep networks in GAP [27], the SRN plays role of a “deep denoiser”, modulating the signal to desired domains [1]. Such a combination brings about following advantages: 1) GAP framework enables competitive performance on video SCI [27]. 2) Under the GAP framework, distinct network structures, *i.e.*, AutoEncoder, U-Net, ResNet and DnCNN [61] are previously utilized, providing adequate references for underlying comparison. 3) The performance of this compound method largely depends on the backbone being applied. While existing structures enables unsatisfactory results. 4) Besides, the well-defined architecture of SRN brings advantage in signal modulation under GAP framework, considering the denoising nature of the modulation and effectiveness of residual learning in denoising [61]. 5) When jointly considered, the combination of SRN and GAP framework could explicitly abstract spatial spectral correlations in diverse signal domains.

Recall that the forward model given in Section 3.1 is applicable to the video SCI. Accordingly, considering the mathematical model in Eq. (3), GAP-net iteratively optimizes the signal, to solve the following objective

$$\hat{\mathbf{f}} = \arg \min_{\mathbf{f}} \frac{1}{2} \|\mathbf{y} - \Phi \mathbf{f}\|_2^2 + \pi \Omega(\mathbf{f}), \quad (18)$$

where  $\Omega(\mathbf{f})$  denotes the regularization term constraining the signal domain. By investigating the augmented Lagrangian formulation [62] of the objective, the GAP-net iteratively solves the Eq. (18) in two steps: 1) linear projection and 2) solving nonlinear shrinkage function by a denoising network. As shown in Fig. 5, it contains  $S$  repeated backbones as denoising networks concatenated by linear projections:

$$\mathbf{f}^{(s+1)} = \mathbf{v}^{(s)} + \Phi^T (\Phi \Phi^T)^{-1} (\mathbf{y} - \Phi \mathbf{v}^{(s)}), \quad (19)$$

where  $\mathbf{v}^{(s)}$  is an auxiliary variable to express the network output of the  $s$ -th network, which prepares the input  $\mathbf{f}^{(s+1)}$  for the  $(s+1)$ -th network. Let  $f_{\text{SRN}}$  again represents the denoising mapping, the backbones essentially work as  $\mathbf{f}^{(s+1)} = f_{\text{SRN}}(\mathbf{v}^{(s)})$ . The above two steps consist of one stage in the unfolding procedure. Notably, the initial input is defined as  $\mathbf{v}^{(0)} = \Phi^T \mathbf{y}$ .

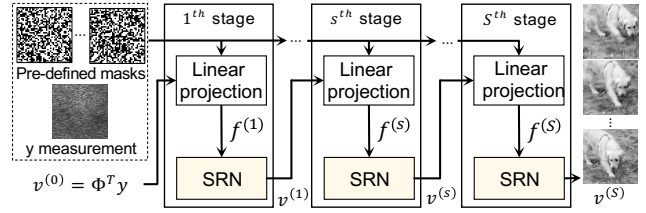


Fig. 5: Structure of GAP-SRN. It takes the measurement  $\mathbf{y}$  and pre-defined masks as input. The framework consists of  $S$  stages. Each stage computes  $\mathbf{f}^{(s)}$  by Eq. (19) and estimates  $\mathbf{v}^{(s)}$  by SRN.  $\Phi$  is determined by masks in Eq. (2). We train the model end-to-end.

---

#### Algorithm 1: Optimization of GAP-SRN

---

**Input:** All parameters of  $S$  SRN:  $\Theta$ ; learning rate  $\eta$ ; Masks; Total  $N$  pairs of measurements and ground truths  $\{\mathbf{y}_n, \mathbf{f}_n\}_{n=1}^N$

**Output:**  $\Theta^*$

- 1 Obtain the sensing matrix  $\Phi$  upon masks by Eq. (2);
- 2 Initialize  $\mathbf{v}_n^{(0)} = \Phi^T \mathbf{y}_n$ ;
- 3 **while not converged do**
- 4     **for**  $s = 1, \dots, S$  **do**
- 5         Compute  $\mathbf{f}^{(s)}$  by Eq. (19);
- 6     **end**
- 7     **for**  $n = 1, \dots, N$  **do**
- 8          $\Theta \leftarrow \Theta - \eta \frac{\partial}{\partial \Theta} \mathcal{L}(\Theta; \mathbf{f}_n, \mathbf{y}_n)$ ;
- 9     **end**
- 10 **end**

---

**Model Training.** The denoiser minimizes the distortion between the input and output. Thus, we have loss

$$\mathcal{L}(\Theta, \mathbf{f}, \mathbf{y}) = \sum_{i=0}^{S-2} \alpha_i \|\mathbf{f} - \mathbf{v}^{(S-i)}\|_2, \quad (20)$$

s.t.  $\mathbf{v}^{(S-i)} = h(\theta; \mathbf{f}^{(S-i-1)})$ ,

where  $\mathbf{f}$  is the ground truth,  $h(\cdot)$  denotes arbitrary SRN with parameter  $\theta_j$  and total parameters  $\Theta = \{\theta_j\}_{j=1}^S$ . We apply the same functional form as [27], where multiple stage (*i.e.*,  $S-2 \sim S$ th stages) outputs are involved in the loss for a better reconstruction. The  $\alpha_0, \alpha_1, \alpha_2$  are 1, 0.5, 0.5, respectively. A pleasing result can be expected by training the model for sufficient iterations. We give the optimization procedure in Algorithm 1.

## 4 Experiments

In this section, we evaluate the proposed method on both spectral and video data. We design the empirical evaluations for answering the following questions:

- How does the proposed CAE-SRN compare against the state-of-the-art in spectral SCI? (Section 4.2)
- Besides the reconstruction performance, what are the further advantages the proposed simple structure brings about for spectral SCI? (Section 4.3)

Table 1: PSNR (dB) comparison on 10 scenes in the simulation dataset. By default, the CAE-SRN represents the SRN enhanced by channel attention but without rescaling pairs, which achieves the state-of-the-art performance.

Method	Scene1	Scene2	Scene3	Scene4	Scene5	Scene6	Scene7	Scene8	Scene9	Scene10	Avg.
U-net [46]	28.28	24.06	26.02	36.33	25.51	27.97	21.15	26.83	26.13	25.07	26.80
HSSP [63]	31.07	26.30	29.00	38.24	27.98	29.16	24.11	27.94	29.14	26.44	28.93
$\lambda$ -net [8]	30.82	26.30	29.42	37.37	27.84	30.69	24.20	28.86	29.32	27.66	29.25
TSA-Net [7]	31.26	26.88	30.03	39.90	28.89	31.30	25.16	29.69	30.03	28.32	30.24
GSM [28]	32.38	27.56	29.02	36.37	28.56	32.49	25.19	31.06	29.40	30.74	30.28
PnP-DIP-HSI [9]	32.70	27.27	31.32	40.79	29.81	30.41	28.18	29.45	34.55	28.52	31.30
GAP-net [27]	33.62	30.08	<b>33.07</b>	40.94	30.77	33.60	27.41	31.25	<b>33.56</b>	30.36	32.47
CAE-SRN (ours)	<b>34.05</b>	<b>31.13</b>	32.34	<b>41.32</b>	<b>31.67</b>	<b>35.36</b>	<b>28.07</b>	<b>33.41</b>	33.40	<b>31.86</b>	<b>33.26</b>

Table 2: SSIM comparison on 10 scenes in the simulation dataset. By default, the CAE-SRN represents the SRN enhanced by channel attention but without rescaling pairs, which achieves the state-of-the-art performance.

Method	Scene1	Scene2	Scene3	Scene4	Scene5	Scene6	Scene7	Scene8	Scene9	Scene10	Avg.
U-net [46]	0.822	0.777	0.857	0.877	0.795	0.794	0.799	0.796	0.804	0.710	0.803
HSSP [63]	0.852	0.798	0.875	0.926	0.827	0.823	0.851	0.831	0.822	0.740	0.834
$\lambda$ -net [8]	0.880	0.846	0.916	0.962	0.866	0.886	0.875	0.880	0.902	0.843	0.886
TSA-Net [7]	0.887	0.855	0.921	0.964	0.878	0.895	0.887	0.887	0.903	0.848	0.893
GSM [28]	0.920	0.892	0.925	<b>0.970</b>	0.894	0.938	0.898	0.932	0.925	0.934	0.923
PnP-DIP-HSI [9]	0.898	0.832	0.920	<b>0.970</b>	0.903	0.890	0.913	0.885	0.932	0.863	0.901
GAP-net [27]	<b>0.926</b>	<b>0.914</b>	<b>0.944</b>	0.966	0.925	0.936	<b>0.915</b>	0.918	<b>0.937</b>	0.914	0.929
CAE-SRN (ours)	0.925	0.906	0.924	0.969	<b>0.940</b>	<b>0.956</b>	0.871	<b>0.952</b>	<b>0.937</b>	<b>0.937</b>	<b>0.931</b>

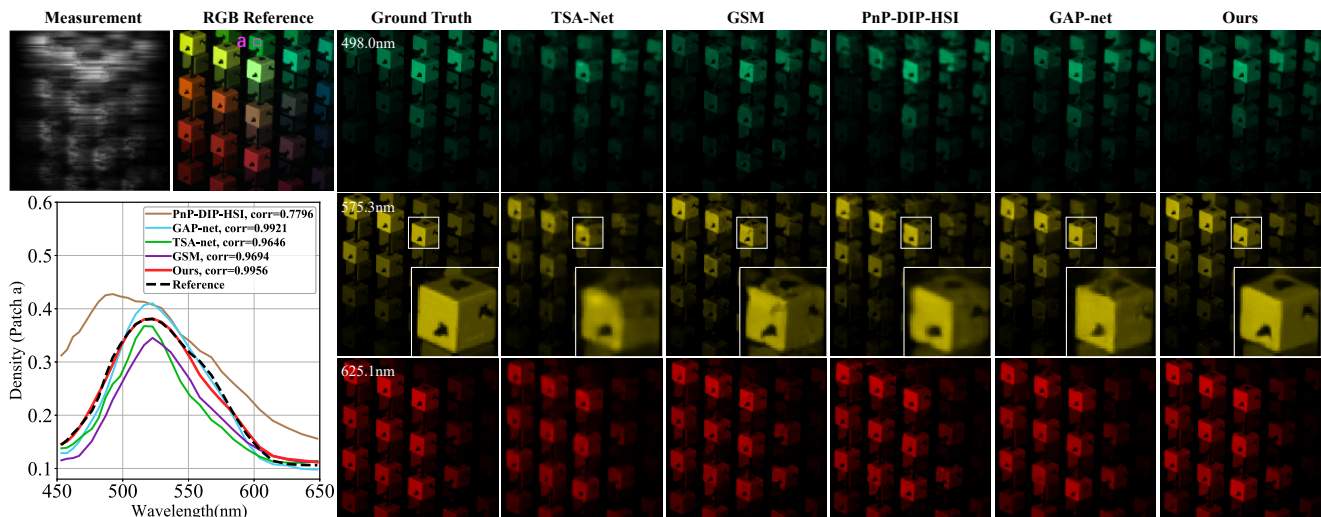


Fig. 6: Comparison of reconstruction results for a synthetic hyperspectral image. Four state-of-the-art methods and our method (right column) are presented on 3 out of 28 spectral channels. The RGB reference is shown to demonstrate the color (top-left). The density-vs-wavelength curves (bottom-left) corresponding to the chosen patch (*i.e.*, patch a) are plotted to demonstrate the spectral fidelity. Our results recover the most details contained in the ground truth, *i.e.*, enlarged windows on 575.3nm wavelength. Please zoom in for a better visualization.

- How does the proposed GAP-SRN compare against the state-of-the-art in video SCI? (Section 4.4)

#### 4.1 Experimental Settings

**Spectral Dataset.** For a fair comparison, we adopt the same 28 wavelengths for the HSI as in [7], distributed within the range of 450nm to 650nm obtained by spectral interpolation manipulation, and conduct experi-

ments on the following two datasets: 1) Simulation Data and 2) Real HSI data. For simulation, both CAVE [64] synthetic dataset and KAIST [65] synthetic dataset are applied in our simulation experiment. For the training set, we create 205 1,024×1,024×28 large image exemplars from 30 256×256×28 images from CAVE dataset by randomly concatenating. Operations like rotation and rescaling are both used for better generalization. During training, we randomly crop 256×256×28 samples from the exemplars. For testing set, ten benchmark

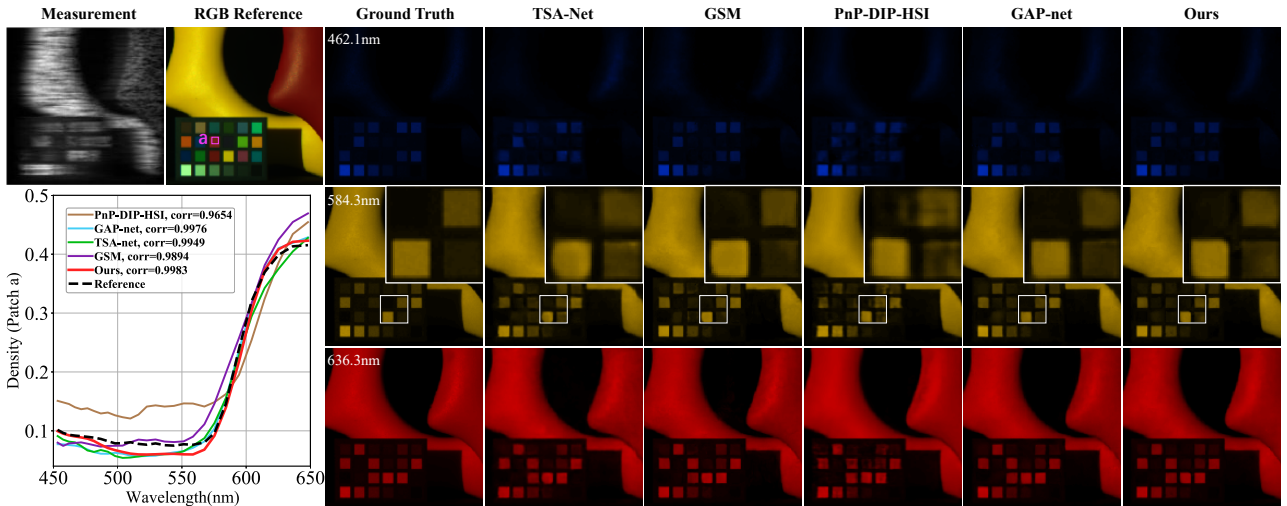


Fig. 7: Comparison of reconstruction results for a synthetic hyperspectral image. Four state-of-the-art methods and our method (right column) are presented on 3 out of 28 spectral channels. The RGB reference is shown to demonstrate the color (top-left). The density-vs-wavelength curves (bottom-left) corresponding to the chosen patch (*i.e.*, patch a) are plotted to demonstrate the spectral fidelity. Our results recover the most details contained in the ground truth, *i.e.*, enlarged windows on 584.3nm wavelength. Please zoom in for a better visualization.

256×256×28 HSIs abstracted from KAIST dataset are applied, following [7, 28]. For real HSI reconstruction, we expand the previous training set by adding 37 HSI images from KAIST [65] dataset. The spatial size of training samples becomes 660×660×28 to be consistent with the real-world measurements, which are obtained by the SD CASSI system developed in [7].

**Video Dataset.** We adopt the DAVIS2017 [66] dataset as the training set of the video SCI. The total number of 26,000 videos of the shape 256×256×8 are generated by data augmentation techniques, *i.e.*, cropping, rotation and downsampling, following [27]. We test the model on benchmark simulation dataset [50], which consists of six videos with the same spatial size (256×256) and different frame numbers, including *Kobe*, *Drop*, *Traffic*, *Aerial*, *Vehicle* and *Runner*.

**Compared Methods.** For spectral SCI, we compare with seven state-of-the-art reconstruction algorithms, including the U-Net [46], HSSP [63],  $\lambda$ -net [8], TSA-Net [7], GSM [28], PnP-DIP-HSI [9] and GAP-net [27] among which the most recent PnP-DIP-HSI and GAP-net demonstrate best performances. For video SCI, we compare with six popular methods on aforementioned benchmark testing set, including GAP-TV [34], E2E-CNN [37], PnP-FFDNet [50], DeSCI [6], BIRNAT [36], GAP-net [27]. Notably, the best-performed GAP-net, GAP-net-Unet-S12, is employed for final performance comparison. Standard validation criterias, Peak Signal-to-Noise Racial (PSNR) and the Structural SIMilarity (SSIM) [67], are used for a quantitative comparison.

The PSNR is computed by

$$\text{PSNR}_{ch} = 10 \log_{10} \left( \frac{\text{MAX}_I^2}{\text{MSE}_{ch}} \right), \quad (21)$$

where we firstly compute the channel-wise PSNR values (*i.e.*,  $\text{PSNR}_{ch}$ ) and then do average. For a certain channel  $ch$ ,  $\text{MAX}_I^2$  denotes the maximum pixel value in ground truth image  $I$ . By default, all PSNR values in this work following this formula.

We implemented our model by PyTorch and employed the Adam optimizer [68] with  $\beta_1=0.9$ ,  $\beta_2=0.999$ . We put 16 Residual Blocks (*i.e.*,  $M=16$ ) in the main body. The learning rate is initialized as  $4 \times 10^{-4}$  and decreased by half every 50 epochs. We set batch size as 4 for the best performance. The training takes at most 16 hours with one NVIDIA TIATN RTX GPU.

## 4.2 Experiments on Sepctral SCI

In this section, we demonstrate the performance of proposed CAE-SRN on both simulation data (Section 4.2.1) and real data (Section 4.2.2). We apply the proposed method on the scenario of high-resolution HSI reconstruction for the first time (Section 4.2.3).

### 4.2.1 HSI Reconstructions on Synthetic Data

We compare with state-of-the-art methods on synthetic HSI data quantitatively and qualitatively. By default, we employ the best-performed model, *i.e.*, CAE-SRN for evaluation, in which each Residual Block contains

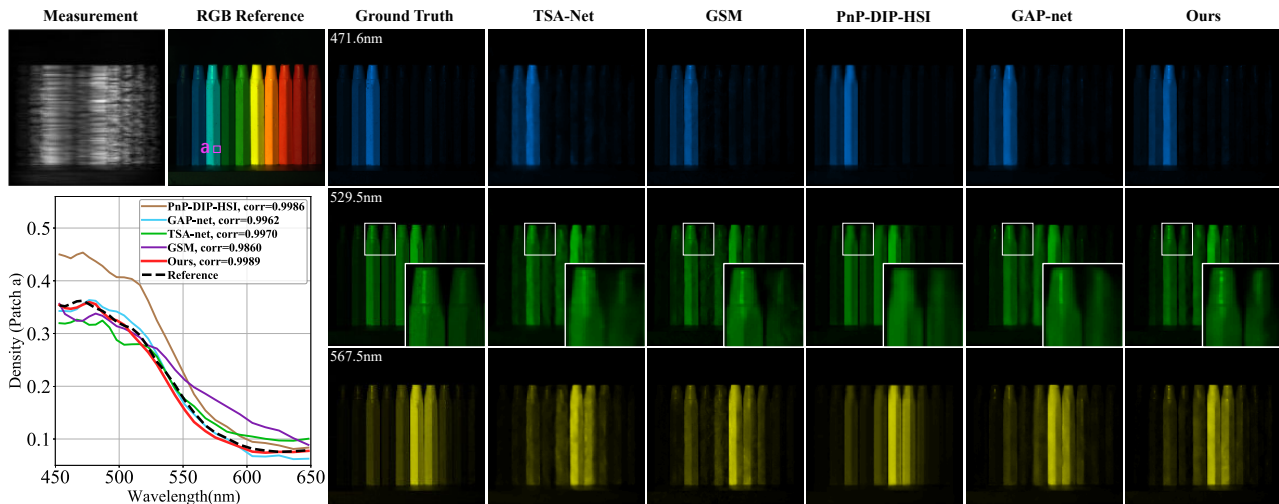


Fig. 8: Comparison of reconstruction results for a synthetic hyperspectral image. Four state-of-the-art methods and our method (right column) are presented on 3 out of 28 spectral channels. The RGB reference is shown to demonstrate the color (top-left). The density-vs-wavelength curves (bottom-left) corresponding to the chosen patch (*i.e.*, patch a) are plotted to demonstrate the spectral fidelity. Our results recover the most details contained in the ground truth, *i.e.*, enlarged windows on 529.5nm wavelength. Please zoom in for a better visualization.

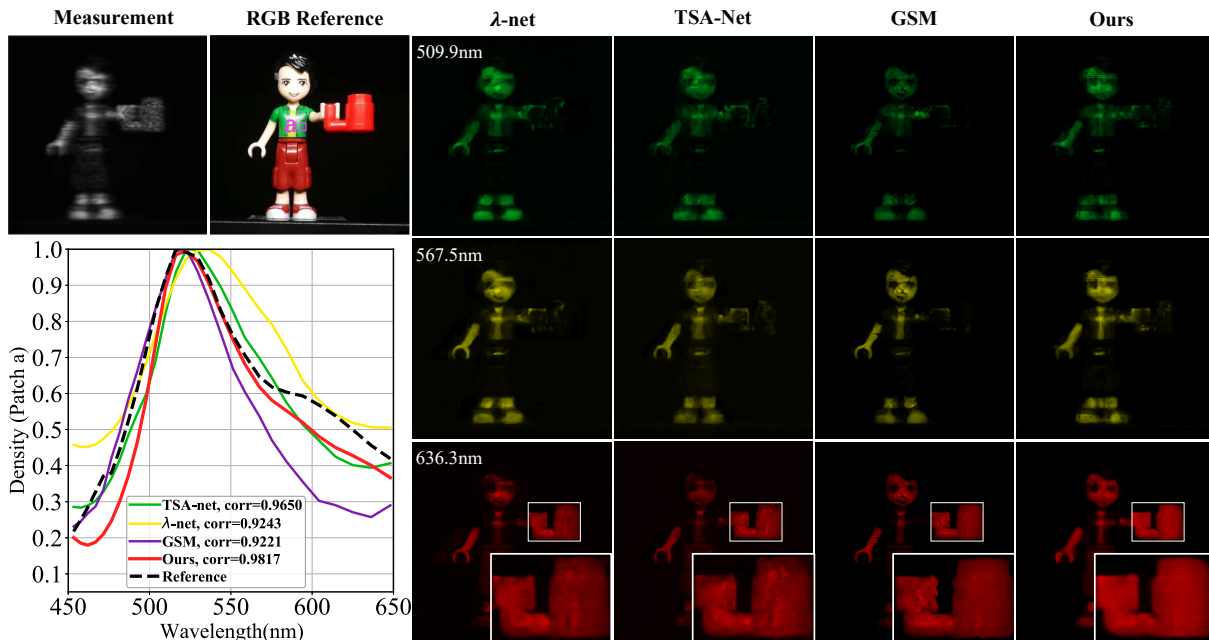


Fig. 9: Comparison of reconstruction results for real-captured hyperspectral signal. The  $\lambda$ -net, TSA-Net, GSM and our method are presented on 3 out of 28 spectral channels. The density-vs-wavelength curves (bottom-left) corresponding to the chosen patch (*i.e.*, patch a) are plotted to demonstrate the spectral fidelity. Notably, we employ the referenced data from a spectrometer provided by [7]. The visual superiority of our method can be demonstrated via observing enlarged windows on 636.3nm wavelength. Please zoom in for a better visualization.

channel attention enhancement module and there are no rescaling pairs introduced. As shown in Table 1 and Table 2, we outperform the others by a large margin. Specifically, we boost around 0.8dB/0.002 compared with the previously best method, GAP-net, in terms of PSNR/SSIM. Besides, we surpass the most recent E2E deep learning model, GSM, by nearly 3dB/0.01

regarding PSNR/SSIM but bearing much less parameters and computations (please refer to Section 4.3 for model size comparison). Notably, we evaluate the GSM upon reconstruction results provided by the authors using Eq. 21, which leads to updated PSNR values. Overall, the comparison indicates that solely applying

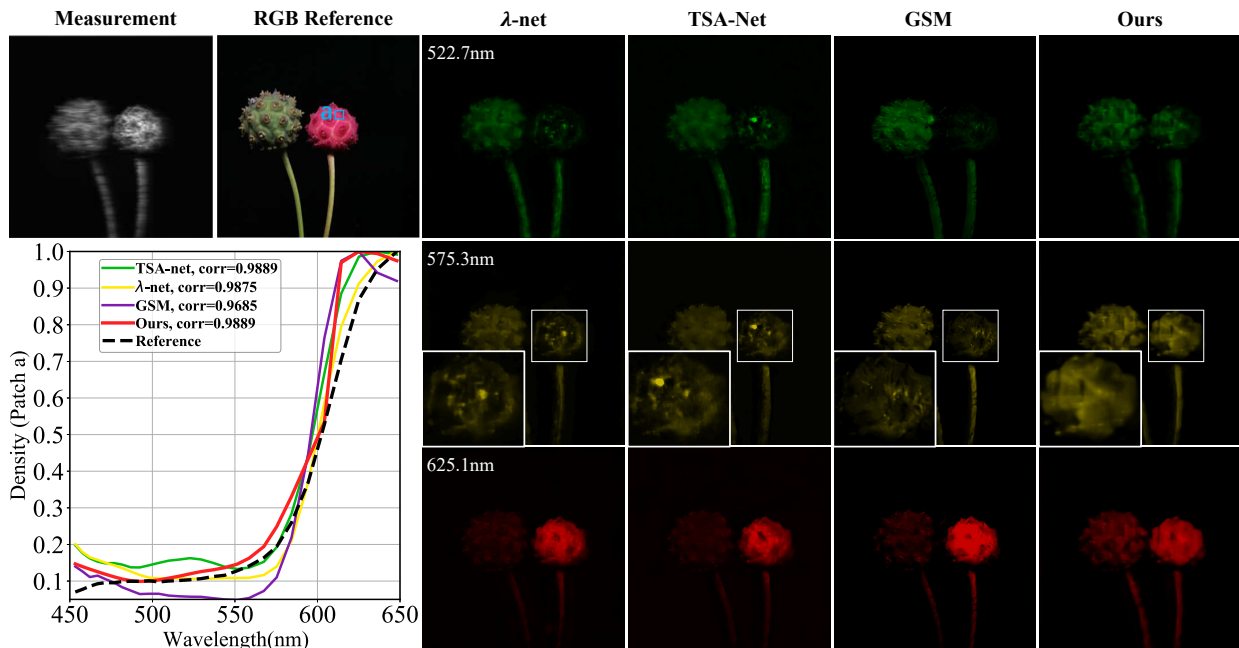


Fig. 10: Comparison of reconstruction results for real-captured hyperspectral signal. The  $\lambda$ -net, TSA-Net, GSM and our method are presented on 3 out of 28 spectral channels. The density-vs-wavelength curves (bottom-left) corresponding to the chosen patch (*i.e.*, patch a) are plotted to demonstrate the spectral fidelity. Notably, we employ the referenced data from a spectrometer provided by [7]. The visual superiority of our method can be demonstrated via observing enlarged windows on 575.3nm wavelength. Please zoom in for a better visualization.

the proposed reconstruction backbone already enables a quantitatively well performance.

We further visualize the reconstruction results by 4 out of 7 best methods and ours in Fig. 6~8. For each visualization, we randomly choose 3 out of 28 spectral channels due to the limited space. Compared with the ground truth, we perceptually retrieve the most textures but introducing the least artifacts and distortion. This can be easily verified by checking enlarged windows at certain spectral channels. As for the other methods, TSA-Net avoids producing artifacts but tends to blur the scene. The GSM is good at reconstructing edges but may generate extra cracks. The PnP-DIP-HSI works globally well but shows instability among different regions. We also evaluate the spectra fidelity by plotting and comparing density-vs-wavelength curves. In a chosen region, the curves by the proposed method share the most overlaps and similar tendencies with the reference, yielding highest correlation values. Notably, we randomly choose the small patches containing varies colors for plotting, demonstrating the wavelength robustness of the proposed method. All in all, our model clearly exceeds existing methods regarding simulation hyperspectral data. In the next section, we validate the effectiveness of the proposed model on HSI data corresponding to real-world scenes collected by SD CASSI.

#### 4.2.2 HSI Reconstructions on Real Data

We still take the CAE-SRN for real HSI reconstruction. No rescaling pairs are introduced. Unlike the simulation case, it is hard to reproducing plausibly well reconstruction results by other methods through training from scratch. Therefore, we choose the methods with pre-trained models available, resulting in  $\lambda$ -net, TSA-Net and GSM. We perceptually compare different methods by two scenes shown in Fig. 9 and Fig. 10. A quantitative comparison fails as the ground truth real HSI data is inaccessible. Similar to simulation case, we plot the density curves for chosen patches. Note that the referenced curve is computed based on the values detected by a real spectrometer following [7, 9].

Real HSI reconstruction is considered to be challenger than simulation case. The real captured measurements unavoidably contain noise and the images are generally characterized by more visual details in a specific spatial size (*i.e.*, in our case,  $660 \times 660$ ). Bearing these difficulties, existing methods present promising results but with their own drawbacks, respectively. For example, the  $\lambda$ -net contains least details. Some mottled regions could be observed (*i.e.*, stem regions of the plants on 522.7nm wavelength in Fig. 10) in reconstructions by TSA-Net. GSM avoids above problems but may cause overexposure/underexposure problems (*i.e.*, ball regions by GSM in Fig. 10). By comparison,

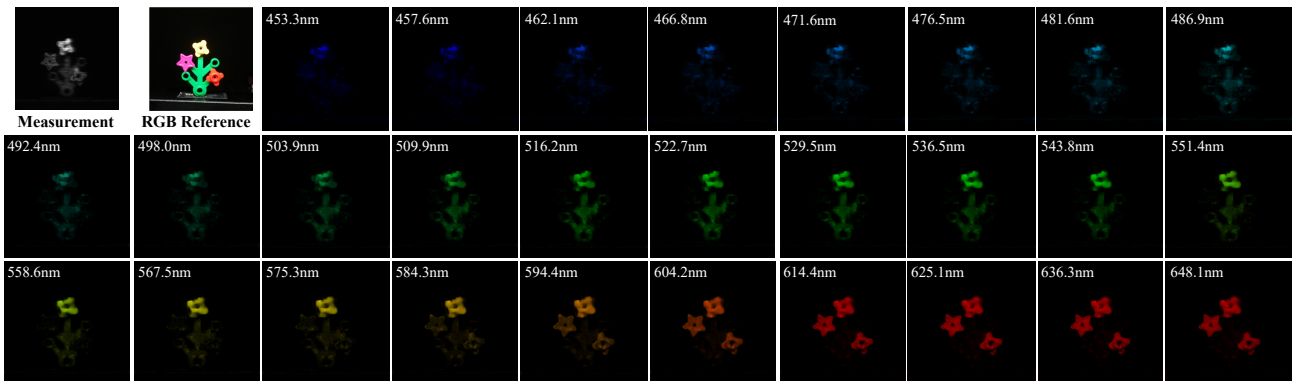


Fig. 11: Reconstruction results for a real-captured hyperspectral signal by the proposed method. Total 28 wavelengths are included. Different channels highlight regions with distinct colors in the RGB reference (top-left).



Fig. 12: Reconstruction of the  $1,024 \times 1,024$  synthetic spectral data by the proposed method. Compared with the ground truth, our method enables fine-grained contents retrieval among diverse wavelengths. Zoom in for a better visualization. To our best knowledge, this is the first exhibition of the reconstruction over such a spatial scale.

our method comprehensively reconstructs the original scene with less artifacts, more details and proper brightness (*i.e.*, enlarged windows in Fig. 9 and Fig. 10). As for the density curves, note that all methods more or less deviate from the referenced curves, among which our approximated curves are most correlated by shapes and tendencies. In Fig. 11, we provide complete reconstruction results on real-captured scene *lego flower*. As can be seen, differently colored regions are emphasized by distinct wavelengths accordingly, indicating an effective spectral response of proposed method. To sum up, considering the substantial dataset shift between the synthetic training set and the real testing

set, our model possesses a better generalization ability, supported by aforementioned superior performance.

#### 4.2.3 High-resolution HSI Reconstruction

In this section, we perform high-resolution HSI reconstruction (*i.e.*,  $1,024 \times 1,024 \times 28$ ) upon SRN. We build a synthetic high-resolution HSI testing set from the KAIST dataset [65]. Technically, existing methods are all capable of reconstructing HSI with arbitrary spatial size. However, it is practically difficult due to the huge requirement of the computation resource. For example, given an input of  $256 \times 256 \times 28$ , the TSA-Net containing 44.25 million parameters needs over  $8 \times 10^{10}$  computations (see detailed discussion on computation in Sec-

Table 3: Model size, computation and performance comparison. The spatial size of the input is  $256 \times 256$ . The annotation v1: w/o rescaling pair, v2: with 1 rescaling pair, v3: with 2 rescaling pairs and CAE: channel attention enhancement. All the other settings are kept the same for a fair comparison.

Method	#params (M)	FLOPs (G)	PSNR (dB)
U-net [46]	31.32	58.99	26.80
$\lambda$ -net [8]	62.64	117.98	29.25
TSA-Net [7]	44.25	80.08	30.24
GSM [28]	3.76	646.35	30.28
SRN v1	<b>1.25</b>	81.84	<b>33.17</b>
SRN v2	1.44	25.07	31.77
SRN v3	1.62	<b>18.57</b>	31.36
CAE-SRN v1	<b>1.31</b>	81.84	<b>33.26</b>
CAE-SRN v2	1.49	25.07	32.33
CAE-SRN v3	1.68	<b>18.57</b>	32.07

Table 4: Discussion on number of Residual Blocks. All the other settings are kept the same for a fair comparison. No rescaling pairs are involved in the model.

#Residual Blocks	PSNR (dB)	SSIM
8	32.02	0.908
12	32.75	0.924
16	33.17	0.929

Table 5: Robustness to real masks by different methods. The settings include **one-to-one**: training/testing model upon identical mask, **one-to-many**: models trained by the same mask are tested by diverse masks and **many-to-many**: training/testing the model with random masks. We report (averaged) PSNR (dB) and perform 100 trials for random testing.

Method	one-to-one	one-to-many	many-to-many
TSA-Net	30.24	27.47 $\pm$ 0.46	21.42 $\pm$ 0.07
GSM	30.28	26.34 $\pm$ 0.06	28.20 $\pm$ 0.01
Ours	33.17	30.17 $\pm$ 0.63	32.24 $\pm$ 0.10

tion 4.3), leading to 18.7Gb GPU memory take-up. For an input of  $1,024 \times 1,024 \times 28$ , the model size remain unchanged while the computation amount would exceed  $1 \times 10^{12}$ . Even two 24Gb GPUs fails to support such a computation. By comparison, the SRN with smaller computation burden makes high-resolution HSI reconstruction more feasible. We compare the reconstruction with the ground truth upon 16 out of 28 spectral channels in Fig. 12. The proposed backbone continuously produces plausible results under a large spatial size. In Fig. 13, we visually present more reconstruction results on random spectral channels. We globally produce plausible results with fine-grained textures as the ground truth. As compared by enlarged windows, the difference between ours and the ground truths are imperceptible, showcasing the strong reconstruction capacity

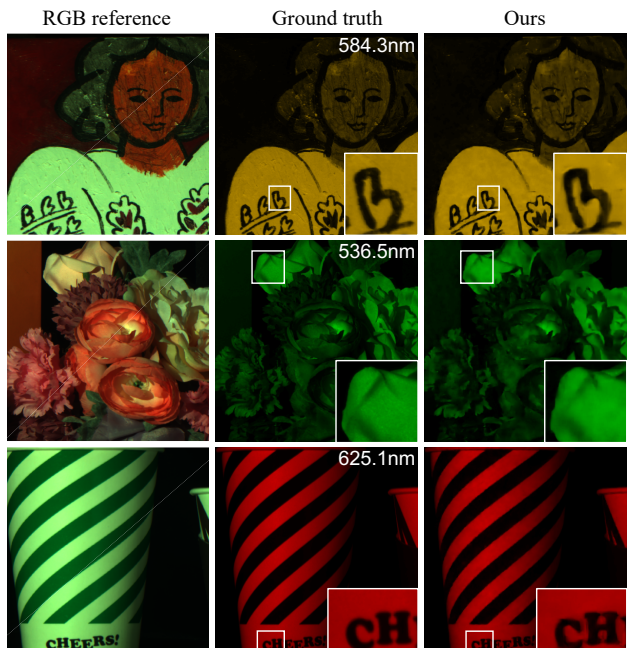


Fig. 13: Visualization of  $1,024 \times 1,024$  HSI reconstruction. By enlarged windows, the proposed method (right column) could produce plausible visual details compared with the ground truth (middle column). RGB reference (left column) are shown to present the color.

of the proposed backbone toward high-resolution HSIs. To our best knowledge, this is the first display of reconstructed spectral data with over 1000-pixel spatial scale and a large spectral channel number.

### 4.3 Model Discussion

In this section, we analysis key components upon simulated spectral data by ablation studies and uncover some advantages attributing to the simple network.

**Ablation Study.** We perform two ablation studies to verify the effectiveness of the key components. Firstly, we focus on the validity of the channel attention module by comparing between SRN and CAE-SRN among three versions, *i.e.*, v1: both introduce no rescaling pair, v2: both equally contain one rescaling pair, v3: both equally apply two rescaling pairs. As shown in Table 3, the channel attention enhancement (CAE) module facilitates evident performance boosts over the latter two versions, *i.e.*, 0.56dB/0.71dB by comparing with the single SRN over v2/v3 models. Notably, only a slight performance boost (0.09dB) can be observed by comparing with two v1 models. Therefore, one can derive a more intuitive conclusion by jointly considering three versions – the CAE module serves as a remedy for performance descent caused by rescaling pairs. This is consistent with the discovery revealed by [32] as we previously mentioned in Section 3.3. In conclusion, the CAE

Table 6: PSNR (dB) and SSIM values by different algorithms on 6 benchmark simulation video data. The proposed SRN is employed as a deep reconstruction backbone for the unfolding framework GAP, denoted by **GAP-SRN**.

Method	Kobe		Traffic		Runner		Drop		Vehicle		Aerial		Average	
	PSNR	SSIM	PSNR	SSIM	PSNR	SSIM	PSNR	SSIM	PSNR	SSIM	PSNR	SSIM	PSNR	SSIM
GAP-TV [34]	26.46	0.885	20.89	0.715	28.52	0.909	34.63	0.970	24.82	0.838	25.05	0.828	26.73	0.858
E2E-CNN [37]	29.02	0.861	23.45	0.838	34.43	0.958	36.77	0.974	26.40	0.886	27.52	0.882	29.26	0.900
PnP-FFDNet [50]	30.50	0.926	24.18	0.828	32.15	0.933	40.70	0.989	25.42	0.849	25.27	0.829	29.70	0.892
DeSCI [6]	<b>33.25</b>	0.952	28.72	0.925	<b>38.76</b>	0.969	43.22	0.993	25.33	0.860	27.04	0.909	32.72	0.935
GAP-net-Unet-S12 [27]	32.09	0.944	28.19	0.929	38.12	0.975	42.02	0.992	27.83	0.931	28.88	0.914	32.86	0.947
BIRNAT [36]	32.71	0.950	29.33	0.942	38.70	0.976	42.28	0.992	27.84	0.927	28.99	0.917	33.31	0.951
GAP-SRN (ours)	32.79	<b>0.954</b>	<b>29.37</b>	<b>0.946</b>	38.66	<b>0.976</b>	<b>43.35</b>	<b>0.999</b>	<b>28.09</b>	<b>0.940</b>	<b>29.31</b>	<b>0.924</b>	<b>33.59</b>	<b>0.959</b>

module contributes to the final performance, especially for the cases with rescaling pairs.

The other fundamental component of the proposed method is the Residual Block (RB). One can simply verify the effectiveness by controlling the number of RBs in SRN network. We exploit three cases including 8, 12 and 16. As reported in Table 4, better performance can be expected with more RBs as there are more parameters included and a larger network depth obtained. Note that the smallest model with 8 RBs achieves over 32dB regarding PSNR, supposing a promising performance of the proposed structure as a lightweight backbone.

**Model Size and FLOPs.** As compared in Table 1, seminal works achieve promising performance in HSI reconstruction. However, one of their problem is the large model size, undermining further deployments to platforms with limited memories. Besides, the giant model volume obstacles the potential incorporation with novel techniques or frameworks, restricting the further development of these insightful works. One possible solution of reducing the model size while maintaining the performance is to employ model compression techniques [69], while operating on the highly specialized structures remains to be quite challenge. By analysis, a compact reconstruction model with a competitive performance is required and our proposed backbone, SRN, properly meets the requirement. In Table 3, we compare the model size (number of trainable parameters) of popular deep learning-based methods and variants of SRN. Our best model, **CAE-SRN v1**, only takes no more than 35% parameters of GSM while boosts nearly 3dB as for PSNR. By comparing with TSA-Net, we only take less than 3% parameters while enjoy a more significant improvement. Our largest model, **CAE-SRN v3** contains additional 0.43 million parameters due to the channel attention enhancement module and CONV layers in rescaling pairs, which turns out to be negligible.

For different methods, we also measure the Floating-Point Operations (FLOPs). Generally, large model size leads to more computations, *i.e.*, the amount of additions and multiplications, thus resulting in high FLOPs.

In addition, the spatial size of the input also impacts the FLOPs. Recall that in Section 4.2.3 we utilize this property. We report the FLOPs of different methods in Table 3, treating it as a reference for measuring time efficiency. Our best performed model, **CAE-SRN v1**, only takes 12.7% FLOPs of GSM. By introducing rescaling pairs in **CAE-SRN v3**, we achieve 2.9% FLOPs of GSM while obtain over 32dB performance. Besides, the rescaling pairs notably reduce the FLOPs while the CAE module barely induces the computation growth. In summary, carrying small model sizes and extremely low FLOPs, the proposed backbone not only demands an economical memory usage, but also is potentially applicable to latency-demanding scenarios.

**Robustness on Masks.** According to Eq. (3), the forward model of SCI is determined by the sensing matrix based on the real mask. Although previous methods offer satisfying approximations to the inverse model, they suffer from performance degradation when applied to new forward models (optical systems with unseen masks), showcasing constrained robustness on masks. The underlying interpretation is the overconfidence owing to their strong modeling capacities. In contrast, simpler model is less troubled [70]. We compare the robustness on real masks of different methods in Tab. 5. Specifically, for single mask-trained models, we test with random real masks, namely **one-to-many**. To make a further step, we train and test models with random masks, namely **many-to-many**. We name the traditional setting as **one-to-one**. Note that masks for training and testing are disjoint. By conclusion, our model indeed enjoys higher robustness over TSA-Net and GSM, regardless of the training setting on masks. Specifically, training the model with random masks leads to over 2dB improvement, enabling a flexible adaptation of the proposed backbone to multiple optical systems.

#### 4.4 Experiments on Video SCI

In this section, we perform experiments on video SCI by integrating the SRN backbone into the GAP frame-



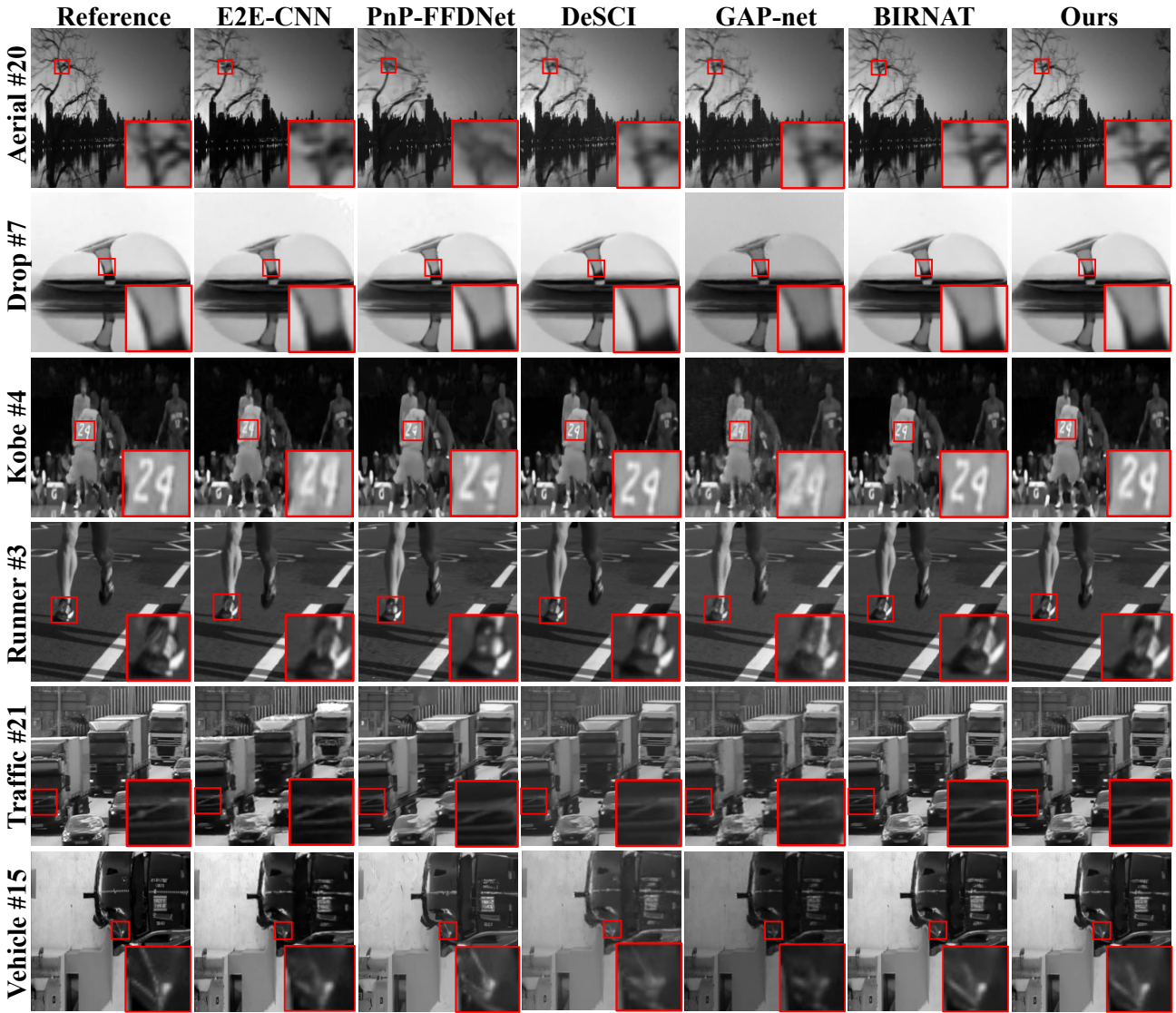


Fig. 14: Reconstruction of the synthetic video data. Methods are demonstrated by random chosen frames. Compared with the ground truth (left column), both BIRNAT [36] and our method recover the most textural details.

work. The performance of the GAP-SRN is analyzed. Similar to spectral SCI, we also uncover the superiority of GAP-SRN on model size and computation burden.

**Performance Comparison.** In Table 6, we report the performance of existing famous methods. By default, we use the SRN containing 16 Residual Blocks and best-performed GAP-net-Unet-S12 (simplified as GAP-Net) throughout the experiment. No rescaling pairs are introduced. We rank first on 4 out of 6 benchmark video data. The SRN is superior than backbone U-Net, which is evidenced by the performance boost over GAP-Net (*i.e.*, 0.73dB/0.012 in terms of PSNR/SSIM). Notably, all the other settings are kept the same for a fair comparison. Besides, we also visualize the reconstructed video frames in Fig. 14, where we exhibit random frames chosen from the video data (rows) and compare six methods (columns). Our method produces

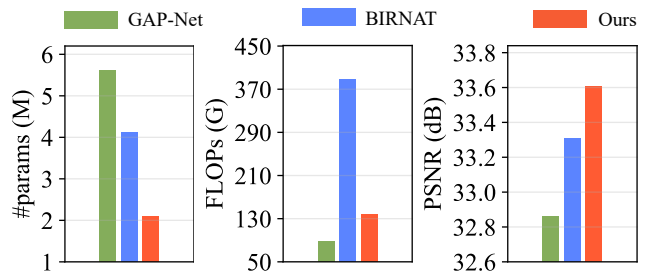


Fig. 15: Comparison between different methods for the video SCI. The model size (*left*) is shown by the amount of parameters ( $\downarrow$ ), the computation burden (*middle*) is measured by FLOPs ( $\downarrow$ ) and the performance (*right*) is indicated by PSNR ( $\uparrow$ ). The proposed method performs best with a smallest model size.

more textures and proper contrast as indicated by the enlarged windows. Note that the BIRNAT shares little

visual difference as ours, which is consistent with the little performance gap between both.

**Model Discussion.** The outstanding performance of GAP-SRN is gained at no cost of the model size. In Fig. 15, we further compare the model size (by the number of parameters), computation burden (by FLOPs) and the performance (by PSNR) of proposed GAP-SRN, GAP-Net and the BIRNAT. For the model size, we only uses half amount of parameters contained in the BIRNAT (*i.e.*, 4.13M v.s. 2.10M). In terms of the computation, both our method and the GAP-net are within the same scale (*i.e.*, around or lower than 130G), while BIRNAT takes 3 times as ours. Notably, we achieve 0.75dB performance improvement by exchanging the backbone in original GAP-net, also exceed BIRNAT by 0.3dB in PSNR. Taken together, we surpass the compared methods in terms of the triple trade-off among model size, computation burden and the performance.

## 5 Conclusion

We have provided a simple yet highly-efficient backbone for the SCI community. The proposed backbone filled the research gap of residual learning-based model design. For the application of HSI, we retrieved the missing visual informative details via exploiting more clues provided by the spectral coherence, leading to CAE-SRN. For video reconstruction, we combined the backbone with a popular unfolding framework, generalized alternating projection (GAP), to produce high-fidelity results and meanwhile, minimize the inference time. On both applications, the leading performances demonstrated the efficiency of the proposed backbone, and the corresponding versatility. We hope the proposed network design with the underlying insights will benefit the future work in the emerging study of SCI.

## References

1. Yuan, X., Brady, D.J., Katsaggelos, A.K.: Snapshot compressive imaging: Theory, algorithms, and applications. *IEEE Signal Processing Magazine* **38**(2) (2021) 65–88 [1](#), [2](#), [9](#)
2. Llull, P., Liao, X., Yuan, X., Yang, J., Kittle, D., Carin, L., Sapiro, G., Brady, D.J.: Coded aperture compressive temporal imaging. *Optics express* **21**(9) (2013) 10526–10545 [2](#), [3](#), [4](#), [6](#)
3. Wagadarikar, A., John, R., Willett, R., Brady, D.: Single disperser design for coded aperture snapshot spectral imaging. *Applied optics* **47**(10) (2008) B44–B51 [2](#), [3](#)
4. Yuan, X., Pang, S.: Structured illumination temporal compressive microscopy. *Biomedical Optics Express* **7**(3) (2016) 746–758 [2](#)
5. He, K., Wang, X., Wang, Z.W., Yi, H., Scherer, N.F., Katsaggelos, A.K., Cossairt, O.: Snapshot multifocal light field microscopy. *Optics express* **28**(8) (2020) 12108–12120 [2](#)
6. Liu, Y., Yuan, X., Suo, J., Brady, D., Dai, Q.: Rank minimization for snapshot compressive imaging. *IEEE Transactions on Pattern Analysis and Machine Intelligence* **41**(12) (Dec 2019) 2990–3006 [2](#), [3](#), [4](#), [11](#), [16](#)
7. Meng, Z., Ma, J., Yuan, X.: End-to-end low cost compressive spectral imaging with spatial-spectral self-attention. In: *European Conference on Computer Vision (ECCV)*. (August 2020) [2](#), [4](#), [5](#), [6](#), [10](#), [11](#), [12](#), [13](#), [15](#)
8. Miao, X., Yuan, X., Pu, Y., Athitsos, V.:  $\lambda$ -net: Reconstruct hyperspectral images from a snapshot measurement. In: *IEEE/CVF Conference on Computer Vision (ICCV)*. (2019) [2](#), [4](#), [7](#), [10](#), [11](#), [15](#)
9. Meng, Z., Yu, Z., Xu, K., Yuan, X.: Self-supervised neural networks for spectral snapshot compressive imaging. In: *Proceedings of the IEEE/CVF International Conference on Computer Vision*. (2021) 2622–2631 [2](#), [4](#), [10](#), [11](#), [13](#)
10. Plaza, A., Benediktsson, J.A., Boardman, J.W., Brazile, J., Bruzzone, L., Camps-Valls, G., Chanussot, J., Fauvel, M., Gamba, P., Gualtieri, A., et al.: Recent advances in techniques for hyperspectral image processing. *Remote sensing of environment* **113** (2009) S110–S122 [2](#)
11. Kim, M.H., Harvey, T.A., Kittle, D.S., Rushmeier, H., Dorsey, J., Prum, R.O., Brady, D.J.: 3d imaging spectroscopy for measuring hyperspectral patterns on solid objects. *ACM Transactions on Graphics (TOG)* **31**(4) (2012) 1–11 [2](#)
12. Xu, Y., Wu, Z., Li, J., Plaza, A., Wei, Z.: Anomaly detection in hyperspectral images based on low-rank and sparse representation. *IEEE Transactions on Geoscience and Remote Sensing* **54**(4) (2015) 1990–2000 [2](#)
13. Borengasser, M., Hungate, W.S., Watkins, R.: *Hyperspectral remote sensing: principles and applications*. CRC press (2007) [2](#)
14. Melgani, F., Bruzzone, L.: Classification of hyperspectral remote sensing images with support vector machines. *IEEE Transactions on geoscience and remote sensing* **42**(8) (2004) 1778–1790 [2](#)
15. Yuan, Y., Zheng, X., Lu, X.: Hyperspectral image super-resolution by transfer learning. *IEEE Journal of Selected Topics in Applied Earth Observations and Remote Sensing* **10**(5) (2017) 1963–1974 [2](#)
16. Yuan, X., Brady, D.J., Katsaggelos, A.K.: Snapshot compressive imaging: Theory, algorithms, and applications. *IEEE Signal Processing Magazine* **38**(2) (2021) 65–88 [2](#), [5](#)
17. Wagadarikar, A., John, R., Willett, R., Brady, D.: Single disperser design for coded aperture snapshot spectral imaging. *Applied Optics* **47**(10) (2008) B44–B51 [2](#)
18. Llull, P., Liao, X., Yuan, X., Yang, J., Kittle, D., Carin, L., Sapiro, G., Brady, D.J.: Coded aperture compressive temporal imaging. *Optics Express* **21**(9) (2013) 10526–10545 [2](#)
19. Wagadarikar, A.A., Pitsianis, N.P., Sun, X., Brady, D.J.: Video rate spectral imaging using a coded aperture snapshot spectral imager. *Optics Express* **17**(8) (2009) 6368–6388 [2](#)
20. Yuan, X., Tsai, T.H., Zhu, R., Llull, P., Brady, D., Carin, L.: Compressive hyperspectral imaging with side information. *IEEE Journal of Selected Topics in Signal Processing* **9**(6) (September 2015) 964–976 [2](#)
21. Wang, L., Sun, C., Zhang, M., Fu, Y., Huang, H.: Dnu: Deep non-local unrolling for computational spectral imaging. In: *Proceedings of the IEEE/CVF Conference on Computer Vision and Pattern Recognition (CVPR)*. (June 2020) [2](#)

22. Wang, L., Xiong, Z., Shi, G., Wu, F., Zeng, W.: Adaptive nonlocal sparse representation for dual-camera compressive hyperspectral imaging. *IEEE Transactions on Pattern Analysis and Machine Intelligence* **39**(10) (Oct 2017) 2104–2111 [2](#)
23. Wang, L., Zhang, T., Fu, Y., Huang, H.: Hyperreconnet: Joint coded aperture optimization and image reconstruction for compressive hyperspectral imaging. *IEEE Transactions on Image Processing* **28**(5) (May 2019) 2257–2270 [2](#)
24. Yuan, X.: Generalized alternating projection based total variation minimization for compressive sensing. In: 2016 IEEE International Conference on Image Processing (ICIP). (Sept 2016) 2539–2543 [2](#), [4](#)
25. Bioucas-Dias, J., Figueiredo, M.: A new TwIST: Two-step iterative shrinkage/thresholding algorithms for image restoration. *IEEE Transactions on Image Processing* **16**(12) (December 2007) 2992–3004 [2](#), [4](#)
26. Wang, L., Xiong, Z., Shi, G., Wu, F., Zeng, W.: Adaptive nonlocal sparse representation for dual-camera compressive hyperspectral imaging. *IEEE transactions on pattern analysis and machine intelligence* **39**(10) (2016) 2104–2111 [2](#)
27. Meng, Z., Jalali, S., Yuan, X.: Gap-net for snapshot compressive imaging. arXiv preprint arXiv:2012.08364 (2020) [2](#), [3](#), [4](#), [5](#), [9](#), [10](#), [11](#), [16](#)
28. Huang, T., Dong, W., Yuan, X., Wu, J., Shi, G.: Deep gaussian scale mixture prior for spectral compressive imaging. In: Proceedings of the IEEE/CVF Conference on Computer Vision and Pattern Recognition. (2021) 16216–16225 [2](#), [4](#), [10](#), [11](#), [15](#)
29. He, K., Zhang, X., Ren, S., Sun, J.: Deep residual learning for image recognition. In: Proceedings of the IEEE conference on computer vision and pattern recognition. (2016) 770–778 [2](#), [4](#)
30. Wang, L., Sun, C., Fu, Y., Kim, M.H., Huang, H.: Hyperspectral image reconstruction using a deep spatial-spectral prior. In: 2019 IEEE/CVF Conference on Computer Vision and Pattern Recognition (CVPR). (June 2019) 8024–8033 [2](#), [4](#)
31. Hu, J., Shen, L., Sun, G.: Squeeze-and-excitation networks. In: Proceedings of the IEEE conference on computer vision and pattern recognition. (2018) 7132–7141 [3](#), [8](#)
32. Zhang, Y., Li, K., Li, K., Sun, G., Kong, Y., Fu, Y.: Accurate and fast image denoising via attention guided scaling. *IEEE Transactions on Image Processing* **30** (2021) 6255–6265 [3](#), [8](#), [15](#)
33. Yuan, X., Llull, P., Liao, X., Yang, J., Brady, D.J., Sapiro, G., Carin, L.: Low-cost compressive sensing for color video and depth. In: Proceedings of the IEEE Conference on Computer Vision and Pattern Recognition. (2014) 3318–3325 [3](#)
34. Yuan, X.: Generalized alternating projection based total variation minimization for compressive sensing. In: 2016 IEEE International Conference on Image Processing (ICIP), IEEE (2016) 2539–2543 [3](#), [11](#), [16](#)
35. Yang, Y., Sun, J., Li, H., Xu, Z.: Deep admm-net for compressive sensing mri. In: Advances in Neural Information Processing Systems 29. (2016) 10–18 [3](#)
36. Cheng, Z., Lu, R., Wang, Z., Zhang, H., Chen, B., Meng, Z., Yuan, X.: Birnat: Bidirectional recurrent neural networks with adversarial training for video snapshot compressive imaging. In: European Conference on Computer Vision, Springer (2020) 258–275 [3](#), [4](#), [11](#), [16](#), [17](#)
37. Qiao, M., Meng, Z., Ma, J., Yuan, X.: Deep learning for video compressive sensing. *APL Photonics* **5**(3) (2020) 030801 [3](#), [4](#), [11](#), [16](#)
38. Yang, J., Yuan, X., Liao, X., Llull, P., Brady, D.J., Sapiro, G., Carin, L.: Video compressive sensing using gaussian mixture models. *IEEE Transactions on Image Processing* **23**(11) (2014) 4863–4878 [3](#)
39. Qiao, M., Liu, X., Yuan, X.: Snapshot spatial-temporal compressive imaging. *Optics letters* **45**(7) (2020) 1659–1662 [3](#)
40. Liao, X., Li, H., Carin, L.: Generalized alternating projection for weighted- $\ell_{2,1}$  minimization with applications to model-based compressive sensing. *SIAM Journal on Imaging Sciences* **7**(2) (2014) 797–823 [3](#), [9](#)
41. Candès, E.J., Romberg, J., Tao, T.: Robust uncertainty principles: Exact signal reconstruction from highly incomplete frequency information. *IEEE Transactions on information theory* **52**(2) (2006) 489–509 [4](#)
42. Donoho, D.L.: Compressed sensing. *IEEE Transactions on information theory* **52**(4) (2006) 1289–1306 [4](#)
43. Reddy, D., Veeraraghavan, A., Chellappa, R.: P2c2: Programmable pixel compressive camera for high speed imaging. In: CVPR 2011, IEEE (2011) 329–336 [4](#)
44. M. A. T. Figueiredo, ., R. D. Nowak, ., Wright, S.J.: Gradient projection for sparse reconstruction: Application to compressed sensing and other inverse problems. (Dec. 2007) 586–597 [4](#)
45. Zheng, S., Liu, Y., Meng, Z., Qiao, M., Tong, Z., Yang, X., Han, S., Yuan, X.: Deep plug-and-play priors for spectral snapshot compressive imaging. *Photon. Res.* **9**(2) (Feb 2021) B18–B29 [4](#)
46. Ronneberger, O., Fischer, P., Brox, T.: U-net: Convolutional networks for biomedical image segmentation. In: International Conference on Medical image computing and computer-assisted intervention, Springer (2015) 234–241 [4](#), [10](#), [11](#), [15](#)
47. Liu, Y., Yuan, X., Suo, J., Brady, D.J., Dai, Q.: Rank minimization for snapshot compressive imaging. *IEEE transactions on pattern analysis and machine intelligence* **41**(12) (2018) 2990–3006 [4](#)
48. Gu, S., Zhang, L., Zuo, W., Feng, X.: Weighted nuclear norm minimization with application to image denoising. In: Proceedings of the IEEE conference on computer vision and pattern recognition. (2014) 2862–2869 [4](#)
49. Boyd, S., Parikh, N., Chu, E.: Distributed optimization and statistical learning via the alternating direction method of multipliers. Now Publishers Inc (2011) [4](#)
50. Yuan, X., Liu, Y., Suo, J., Dai, Q.: Plug-and-play algorithms for large-scale snapshot compressive imaging. In: Proceedings of the IEEE/CVF Conference on Computer Vision and Pattern Recognition. (2020) 1447–1457 [5](#), [11](#), [16](#)
51. Zhang, K., Zuo, W., Zhang, L.: Ffdnet: Toward a fast and flexible solution for cnn-based image denoising. *IEEE Transactions on Image Processing* **27**(9) (2018) 4608–4622 [5](#)
52. Donoho, D.L.: Compressed sensing. *IEEE Transactions on Information Theory* **52**(4) (April 2006) 1289–1306 [5](#)
53. Emmanuel, C., Romberg, J., Tao, T.: Robust uncertainty principles: Exact signal reconstruction from highly incomplete frequency information. *IEEE Transactions on Information Theory* **52**(2) (February 2006) 489–509 [5](#)
54. Zagaruyko, S., Komodakis, N.: Wide residual networks. arXiv preprint arXiv:1605.07146 (2016) [6](#)
55. Szegedy, C., Ioffe, S., Vanhoucke, V., Alemi, A.A.: Inception-v4, inception-resnet and the impact of residual connections on learning. In: Thirty-first AAAI conference on artificial intelligence. (2017) [6](#)
56. He, K., Zhang, X., Ren, S., Sun, J.: Identity mappings in deep residual networks. In: European conference on computer vision, Springer (2016) 630–645 [6](#)

57. Ioffe, S., Szegedy, C.: Batch normalization: Accelerating deep network training by reducing internal covariate shift. In: International conference on machine learning, PMLR (2015) 448–456 [7](#)
58. Luo, W., Li, Y., Urtasun, R., Zemel, R.: Understanding the effective receptive field in deep convolutional neural networks. In: Proceedings of the 30th International Conference on Neural Information Processing Systems. (2016) 4905–4913 [7](#)
59. Shi, W., Caballero, J., Huszár, F., Totz, J., Aitken, A.P., Bishop, R., Rueckert, D., Wang, Z.: Real-time single image and video super-resolution using an efficient sub-pixel convolutional neural network. In: Proceedings of the IEEE conference on computer vision and pattern recognition. (2016) 1874–1883 [8](#)
60. Zhang, Y., Li, K., Li, K., Wang, L., Zhong, B., Fu, Y.: Image super-resolution using very deep residual channel attention networks. In: Proceedings of the European conference on computer vision (ECCV). (2018) 286–301 [8](#)
61. Zhang, K., Zuo, W., Chen, Y., Meng, D., Zhang, L.: Beyond a gaussian denoiser: Residual learning of deep cnn for image denoising. *IEEE transactions on image processing* **26**(7) (2017) 3142–3155 [9](#)
62. Sun, J., Li, H., Xu, Z., et al.: Deep admm-net for compressive sensing mri. *Advances in neural information processing systems* **29** (2016) [9](#)
63. Wang, L., Sun, C., Fu, Y., Kim, M.H., Huang, H.: Hyperspectral image reconstruction using a deep spatial-spectral prior. In: 2019 IEEE/CVF Conference on Computer Vision and Pattern Recognition (CVPR). (June 2019) 8024–8033 [10](#), [11](#)
64. Park, J., Lee, M., Grossberg, M.D., Nayar, S.K.: Multispectral Imaging Using Multiplexed Illumination. In: IEEE International Conference on Computer Vision (ICCV). (Oct 2007) [10](#)
65. Choi, I., Kim, M., Gutierrez, D., Jeon, D., Nam, G.: High-quality hyperspectral reconstruction using a spectral prior. Technical report (2017) [10](#), [11](#), [14](#)
66. Pont-Tuset, J., Perazzi, F., Caelles, S., Arbeláez, P., Sorkine-Hornung, A., Van Gool, L.: The 2017 davis challenge on video object segmentation. *arXiv preprint arXiv:1704.00675* (2017) [11](#)
67. Wang, Z., Bovik, A.C., Sheikh, H.R., Simoncelli, E.P., et al.: Image quality assessment: From error visibility to structural similarity. *IEEE Transactions on Image Processing* **13**(4) (2004) 600–612 [11](#)
68. Kingma, D.P., Ba, J.: Adam: A method for stochastic optimization. *arXiv preprint arXiv:1412.6980* (2014) [11](#)
69. Cheng, Y., Wang, D., Zhou, P., Zhang, T.: A survey of model compression and acceleration for deep neural networks. *arXiv preprint arXiv:1710.09282* (2017) [16](#)
70. Guo, C., Pleiss, G., Sun, Y., Weinberger, K.Q.: On calibration of modern neural networks. In: International Conference on Machine Learning, PMLR (2017) 1321–1330 [16](#)